



# First Chromospheric Activity and Doppler Imaging Study of PW And Using a New Doppler Imaging Code: SpotDIPy

Engin Bahar<sup>1</sup>, Hakan V. Şenavcı<sup>1</sup>, Emre Işık<sup>2,3</sup>, Gaithe A. J. Hussain<sup>4</sup>, Oleg Kochukhov<sup>5</sup>, David Montes<sup>6</sup>, and Yue Xiang<sup>7,8</sup>

<sup>1</sup> Department of Astronomy and Space Sciences, Faculty of Science, Ankara University, Beşevler 06100, Ankara, Türkiye; [enbahar@ankara.edu.tr](mailto:enbahar@ankara.edu.tr)

<sup>2</sup> Max-Planck-Institut für Sonnensystemforschung, Justus-von-Liebig-Weg 3, D-37077 Göttingen, Germany

<sup>3</sup> Department of Computer Science, Turkish-German University, Beykoz 34820, Istanbul, Türkiye

<sup>4</sup> European Space Agency (ESA), European Space Research and Technology Centre (ESTEC), Keplerlaan 1, 2201 AZ Noordwijk, The Netherlands

<sup>5</sup> Department of Physics and Astronomy, Uppsala University, Box 516, SE-75120 Uppsala, Sweden

<sup>6</sup> Departamento de Física de la Tierra y Astrofísica & IPARCOS-UCM (Instituto de Física de Partículas y del Cosmos de la UCM), Facultad de Ciencias Físicas, Universidad Complutense de Madrid, E-28040 Madrid, Spain

<sup>7</sup> Yunnan Observatories, Chinese Academy of Sciences, Kunming 650216, People's Republic of China

<sup>8</sup> Key Laboratory for the Structure and Evolution of Celestial Objects, Chinese Academy of Sciences, Kunming 650216, People's Republic of China

Received 2023 January 19; revised 2023 October 12; accepted 2023 October 12; published 2023 December 22

## Abstract

Measuring the coverage of dark spots on cool stars is important to understanding how stellar magnetic activity scales with the rotation rate and convection zone depth. In this respect, it is crucial to infer surface magnetic patterns on G and K stars, to reveal solar-like stellar dynamos in action. Molecular bands serve as invaluable indicators of cool spots on the surfaces of stars, as they play a crucial role in enabling accurate assessments of the extent of spot coverage across the stellar surface. Therefore, more reliable surface images can be obtained considering the inversion of atomic lines with molecular bands. In this context, we simultaneously carry out Doppler imaging (DI) using atomic lines as well as titanium oxide band profiles of PW And (K2 V) and also investigate chromospheric activity indicators for the first time in the literature, using high-resolution spectra. The surface spot distribution obtained from the inversion process represents both atomic line and TiO-band profiles quite accurately. The chromospheric emission is also correlated with photospheric spot coverage, except during a possible flare event during the observations. We detect frequent flare activity, using TESS photometry. We also introduce a new open-source, Python-based DI code *SpotDIPy* that allows performing surface reconstructions of single stars using the maximum entropy method. We test the code by comparing surface reconstruction simulations with the extensively used *DoTS* code. We show that the surface brightness distribution maps reconstructed via both codes using the same simulated data are consistent with each other.

*Unified Astronomy Thesaurus concepts:* Stellar activity (1580); Doppler imaging (400); Starspots (1572)

## 1. Introduction

PW And is a rapidly rotating pre-main-sequence K2 V-type star, which is a member of the AB Doradus moving group. Its high Li I abundance also confirms its membership in the young Local Association (Montes et al. 2001a, 2001b; López-Santiago et al. 2003; Montes et al. 2004). Its projected rotational velocity,  $v \sin i$ , was determined by several investigators in the literature in the range of  $21.5 \text{ km s}^{-1}$  (Griffin 1992) to  $23.9 \text{ km s}^{-1}$  (Strassmeier & Rice 2006). A detailed activity investigation of PW And was performed by López-Santiago et al. (2003), who analyzed photospheric Ca I and Fe I line profiles using CCF bisector analysis (see Dempsey et al. 1992, for more details) and found that the CCF bisectors change with a period similar to the photometric period of PW And, suggesting the presence of cool spots. Using the spectral subtraction technique (Montes et al. 2000), they also measured the equivalent width (EW) variation of chromospheric activity indicator lines from Ca II H&K to Ca II IRT lines along with the rotational phase and found that the chromospheric regions appear to be associated with the photospheric features obtained using CCF bisector analysis. In addition, they detected two

flares in 2001 and 2002, confirming the strong magnetic activity of the star. López-Santiago et al. (2010) and Lehtinen et al. (2016) determined the emission index as  $\log R'_{\text{HK}} - 3.85$  and  $-4.217$ , respectively, revealing the highly active chromosphere. The first Doppler imaging (DI) of PW And was obtained by Strassmeier & Rice (2006), using high-resolution CFHT spectroscopy. They found that cool spots are located within an equatorial band up to  $\pm 40^\circ$  of the stellar equator, with temperature contrast relative to the immaculate photosphere of up to  $\Delta T = 1200 \text{ K}$ . They also estimated a set of astrophysical parameters (see Table 1 of Strassmeier & Rice 2006, for more details), including the rotation period as 1.76159 days, using high-precision photometry. Another DI analysis was carried out by Gu et al. (2010), who used high-resolution spectra obtained at the Xinglong Station of National Astronomical Observatories and Bohyunsan Astronomical Observatory. Their spectra were separated into two subsets spanning approximately 1 month. Unlike the Doppler images presented by Strassmeier & Rice (2006), their resulting spot distributions were rather concentrated within intermediate to high latitudes, while weaker low-latitude spots were also visible. They also reported that there is no notable position variation of spots and concluded that intermediate- to high-latitude spots have lifetimes longer than a month. Based on the high-resolution spectroscopic observations carried out at the RTT-150 telescope of the TÜBİTAK National Observatory, the



Original content from this work may be used under the terms of the [Creative Commons Attribution 4.0 licence](https://creativecommons.org/licenses/by/4.0/). Any further distribution of this work must maintain attribution to the author(s) and the title of the work, journal citation and DOI.

most recent DI was performed by Kolbin & Galeev (2017). They found that spots were located around a latitude of  $40^\circ$  and claimed that the resultant map is similar to that obtained by Strassmeier & Rice (2006), where spots spread between  $0^\circ$  and  $40^\circ$  with a tendency toward  $30^\circ$ .

The latitudinal distributions of spots on PW And that were inferred in previous studies are substantially different from each other. Possible underlying reasons are the image reconstruction process and intrinsic variations of spot distribution on the star between different epochs. New observations carried out at different epochs are thus needed to improve the basic statistics of the latitudinal spot distribution. Another reason for reexamining PW And, apart from previous DI studies based on atomic lines, is to simultaneously confirm the spot distribution and contrast using TiO-band at  $7055 \text{ \AA}$  in this research.

In this study, we conducted a simultaneous analysis of both atomic line and TiO-band profiles with the DI technique on PW And, using three distinct sets of observations spanning different time intervals. Concurrently, we investigated chromospheric activity within the same data set and compared the observed activity trends. Additionally, an accurate rotation period of PW And was calculated using the Lomb–Scargle periodogram, and  $v \sin i$  was determined on a 2D grid search. We also introduced a new open-source and user-friendly Python-based DI code `SpotDIPy` and tested via `DoTS` (Collier Cameron 1992).

## 2. Observations and Data Reduction

We obtained a high-resolution spectral time series of PW And, using the HERMES<sup>9</sup> spectrograph (Raskin et al. 2011) attached to the 1.2 m Mercator telescope at the Roque de los Muchachos Observatory (La Palma, Spain), between 2015 December 14 and 19 (hereafter Set 1), 2018 September 25–29 (hereafter Set 2) and 2018 December 14–19 (hereafter Set 3). Consequently, Sets 1–3 data of PW And obtained in this study cover approximately 2.9, 2.4, and 2.3 rotational cycles, respectively.

The average spectral resolution is  $R = 85,000$  with a wavelength coverage between  $3780$  and  $9007 \text{ \AA}$ . The data were acquired using exposure times between  $1200$  and  $1800 \text{ s}$ , which yielded signal-to-noise ratios (S/Ns) between  $73$  and  $174$ . The S/N values of the spectra are given as per pixel around  $550 \text{ nm}$ . The effective spectral resolution is between  $0.045$  and  $0.106 \text{ \AA}$  in wavelength and  $3.5 \text{ km s}^{-1}$  in velocity units, while the sampling is  $2$  pixels per resolution element. The log of the HERMES observing run is given in Table 1. The reduction of the spectra was performed using the automatic pipeline of the spectrograph (Raskin et al. 2011). The pipeline was utilized to execute fundamental echelle data reduction procedures, encompassing tasks, such as bias, flat-field, and inter-order background level corrections, as well as the extraction of 1D spectra and subsequent wavelength calibration. The normalization procedure was carried out via a Python code developed by our working group (Şenavcı et al. 2018).

We used the multiline technique, least-squares deconvolution (LSD; Donati et al. 1997) to produce a mean photospheric line profile with higher S/N, in turn improving the quality of the resulting spot maps. The line mask contains information on the line positions and relative strengths and is required to

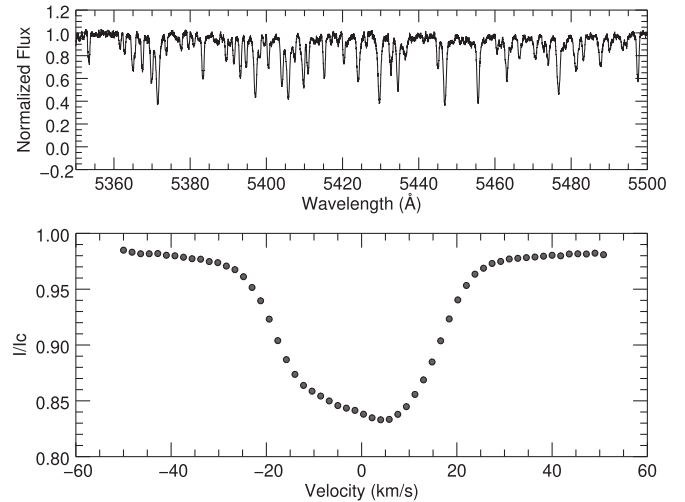


**Figure 1.** The input spectrum (top panel) and the resultant LSD profile (bottom panel) of PW And, corresponding to the rotational phase 0.002 of Set 1. Note that only part of the input spectrum is shown here for better visualization.

**Table 1**  
Phase-ordered Spectroscopic Observation Log of PW And

| Date       | Exp. Time<br>(s) | BJD <sub>Mid</sub> | Phase <sub>Mid</sub> | S/N |
|------------|------------------|--------------------|----------------------|-----|
| 18.12.2015 | 1800             | 57375.45063        | 0.002                | 108 |
| 15.12.2015 | 1200             | 57372.32557        | 0.223                | 74  |
| 19.12.2015 | 1800             | 57376.30420        | 0.488                | 77  |
| 19.12.2015 | 1800             | 57376.32584        | 0.500                | 73  |
| 19.12.2015 | 1800             | 57376.47665        | 0.586                | 104 |
| 14.12.2015 | 1600             | 57371.33483        | 0.659                | 92  |
| 16.12.2015 | 1800             | 57373.31890        | 0.788                | 102 |
| 18.12.2015 | 1800             | 57375.30685        | 0.920                | 108 |
| <hr/>      |                  |                    |                      |     |
| 25.09.2018 | 1500             | 58387.36672        | 0.066                | 155 |
| 25.09.2018 | 1500             | 58387.45742        | 0.117                | 172 |
| 27.09.2018 | 1500             | 58389.40298        | 0.225                | 119 |
| 27.09.2018 | 1500             | 58389.47599        | 0.266                | 142 |
| 29.09.2018 | 1500             | 58391.39726        | 0.360                | 170 |
| 29.09.2018 | 1500             | 58391.50205        | 0.420                | 174 |
| 26.09.2018 | 1500             | 58388.40970        | 0.659                | 169 |
| 27.09.2018 | 1500             | 58388.51470        | 0.719                | 169 |
| <hr/>      |                  |                    |                      |     |
| 15.12.2018 | 1600             | 58468.35045        | 0.168                | 79  |
| 17.12.2018 | 1600             | 58470.31374        | 0.286                | 154 |
| 17.12.2018 | 1600             | 58470.43395        | 0.354                | 161 |
| 18.12.2018 | 1200             | 58470.51817        | 0.402                | 135 |
| 14.12.2018 | 1600             | 58467.44046        | 0.650                | 105 |
| 16.12.2018 | 1600             | 58469.35515        | 0.740                | 111 |
| 16.12.2018 | 1600             | 58469.46048        | 0.800                | 126 |
| 18.12.2018 | 1200             | 58471.31222        | 0.854                | 140 |
| 18.12.2018 | 1200             | 58471.43170        | 0.922                | 144 |
| 19.12.2018 | 1200             | 58471.51305        | 0.968                | 129 |

construct the mask used by LSD. We extracted the line mask from the Vienna Atomic Line Database (VALD; Kupka et al. 1999). The wavelength regions including lines that are affected by chromospheric heating (i.e., hydrogen Balmer series, Na I (D<sub>1</sub>, D<sub>2</sub>), Ca II IRT) and strong telluric lines were removed from the list to prevent any artifacts in the LSD profiles. We set the velocity increment to  $1.75 \text{ km s}^{-1}$ , considering spectral resolution ( $3.5 \text{ km s}^{-1}$ ) and its sampling ( $2$ ) in pixels. We obtained LSD profiles of PW And with an S/N in the range

<sup>9</sup> Based on observations obtained with the HERMES spectrograph mounted on the 1.2 m Mercator Telescope at the Spanish Observatorio del Roque de los Muchachos of the Instituto de Astrofísica de Canarias.

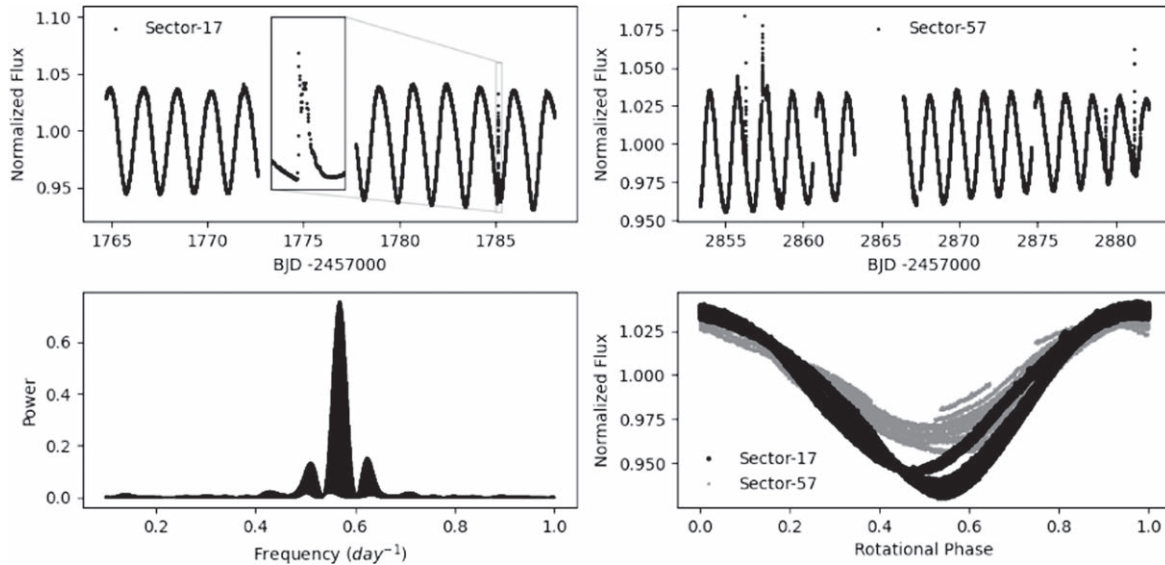


**Figure 2.** Top panel: TESS light curves in Sector 17 (left) and in Sector 57 (right). Bottom panel: Lomb–Scargle periodogram (left) and phase-folded light curves (right) using the period determined from the periodogram, for Sector 17 (black circles) and Sector 57 (gray circles).

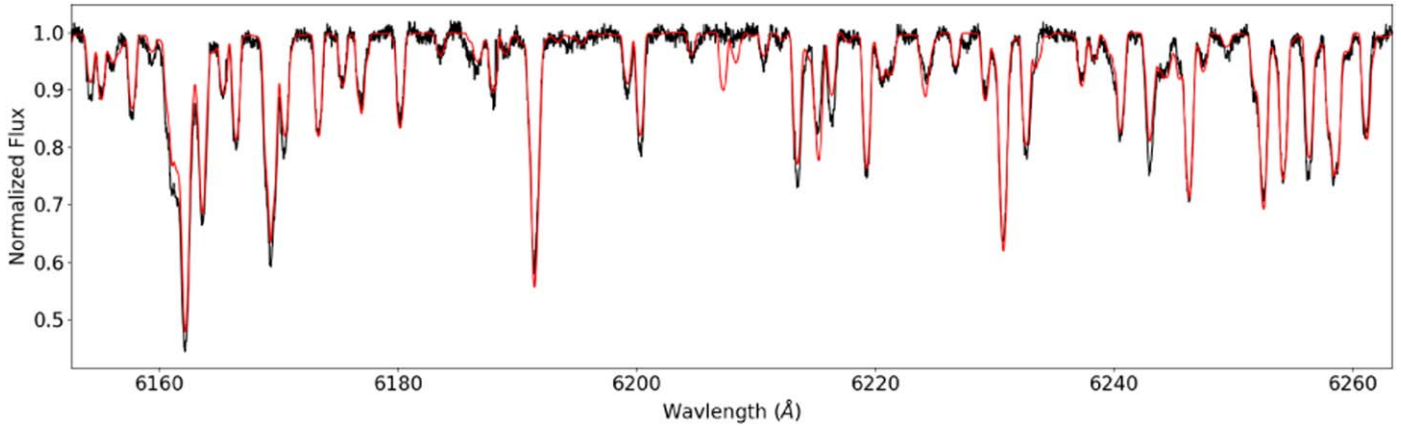


**Figure 3.** A comparison of the observed spectrum of PW And (black) with the best-fit model (red) obtained through the spectral synthesis fitting method.

between 670 and 850. An example of part of an input spectrum and the resultant LSD profile is shown in Figure 1.

The Transiting Exoplanet Survey Satellite (TESS; Ricker et al. 2015) photometry of PW And enabled us to determine the rotation period with high precision. TESS observed PW And in sectors 17 and 57, corresponding to time spans of 2019 October 8–November 2 and 2022 September 30–October 29, respectively. All of the light-curve data presented in this paper were obtained from the Mikulski Archive for Space Telescopes (MAST<sup>10</sup>) at the Space Telescope Science Institute. The specific observations analyzed can be accessed via DOI:10.17909/g29a-2t15. Among the two types of photometric data available, SAP flux is generated by summing all pixel values in a predefined aperture as a function of time, while PDCSAP flux is SAP flux from which long-term trends have been removed, using the so-called co-trending basis vectors. Since there is no amplitude difference between SAP and PDCSAP light-curve data, we used the latter one to determine the rotation period of PW And.

### 3. Analysis

#### 3.1. Rotation Period Estimation

Although the TESS sectors 17 and 57 are about 3 yr apart, the light-curve morphology remains almost the same in both sectors as a dominant sinusoidal variation. This is shown in Figure 2 (upper panels). To investigate periodicities owing to the rotational modulation by spots, we computed the Lomb–Scargle periodogram, using the light curves from both sectors, after removing outliers and flares. The periodogram shows a clear peak (Figure 2, lower left panel), corresponding to  $0.569280 \text{ days}^{-1}$  in the frequency domain and  $1.756604 \pm 0.000015 \text{ days}$  in the period domain. The period and its associated uncertainty were determined by fitting the peak using a Gaussian function through the least-squares method, along with the application of the bootstrap method. The resultant period is close to 1.76159 days obtained by Strassmeier & Rice (2006). The phase-folded light curves in Figure 2 show that the Sector 17 data has a higher amplitude compared to Sector 57, while both sector data show similar modulations. All the photometric and spectroscopic data used

<sup>10</sup> <https://mast.stsci.edu>

**Table 2**  
Adopted Stellar Parameters

| Parameter                        | Value   |
|----------------------------------|---|
| $v \sin i$ [km s <sup>-1</sup> ] | 21.4 <sup>+1.0</sup> <sub>-0.8</sub> <sup>a</sup> |
| $M$ [ $M_{\odot}$ ]              | 0.85 ± 0.05 <sup>b</sup>                          |
| $i$ [°]                          | 46.0 ± 7 <sup>c</sup>                             |
| $P_{\text{rot}}$ [day]           | 1.756604 ± 0.000015 <sup>a</sup>                  |
| $T_0$ [HJD]                      | 2453200.0 <sup>c</sup>                            |
| $T_{\text{eff}}$ [K]             | 5080 ± 28 <sup>a</sup>                            |
| $T_{\text{spot}}$ [K]            | 3800 <sup>c</sup>                                 |
| log $g$                          | 4.40 ± 0.09 <sup>a</sup>                          |
| [Fe/H]                           | -0.14 ± 0.02 <sup>a</sup>                         |
| $\xi$ [km s <sup>-1</sup> ]      | 1.93 ± 0.09 <sup>a</sup>                          |
| $\zeta$ [km s <sup>-1</sup> ]    | 3.25 ± 0.06 <sup>a</sup>                          |

**Notes.**

<sup>a</sup> This study.

<sup>b</sup> Folsom et al. (2016).

<sup>c</sup> Strassmeier & Rice (2006).

in the analysis are phased using the following equation:

$$\text{BJD} = 2453200.00 + 1^{\text{d}}.756604 \times E. \quad (1)$$

### 3.2. Stellar Parameters Estimation

We obtained the stellar parameters of PW And using the spectral synthesis fitting method. Synthetic spectra were produced using the SPECTRUM (Gray & Corbally 1994) code with MARCS (Gustafsson et al. 2008) atmosphere models and the VALD line list. The fitting was performed on all Fe I and Fe II lines in the wavelength range of 5400–6800 Å of the stellar spectrum. This region was selected because it contains relatively few telluric lines and the continuum can be more easily detected. All of these operations were carried out through iSpec (Blanco-Cuaresma et al. 2014; Blanco-Cuaresma 2019). The obtained parameters and errors were calculated using the bootstrap method. The resultant parameters are given in Table 2, which is consistent with the parameters recently obtained by Folsom et al. (2016). A comparison of the synthetic spectrum and the observed spectrum is shown in Figure 3.

### 3.3. DI Code: SpotDIPy

To reconstruct the distribution of starspots, we developed a DI code, SpotDIPy, written in the Python programming language. The code generates synthetic line profiles ( $R_{\text{calc}}$ ) by integrating local line profiles across the entire visible stellar surface at each rotational phase,  $\phi$ . Each surface element on the stellar surface consists of two line profiles with different temperatures, one representing the photosphere and the other representing the spots. This is a basic assumption for the DI method based on the two-temperature model with the resulting distribution in terms of spot-filling factors,  $f_s$ , defined as the fraction of the surface element area occupied by spots. During the integration process, local line profiles are shifted and scaled with respect to the position of the surface element in the velocity space and the projected areas, respectively. The local line profiles also are scaled with a continuum flux ratio calculated from blackbody assumption based on their corresponding temperatures and central wavelengths. Limb- and gravity-darkening effects are taken into account during reconstruction. Limb-darkening coefficients are calculated by the Python package, ExoTiC-LD (Grant & Wakeford 2022). The

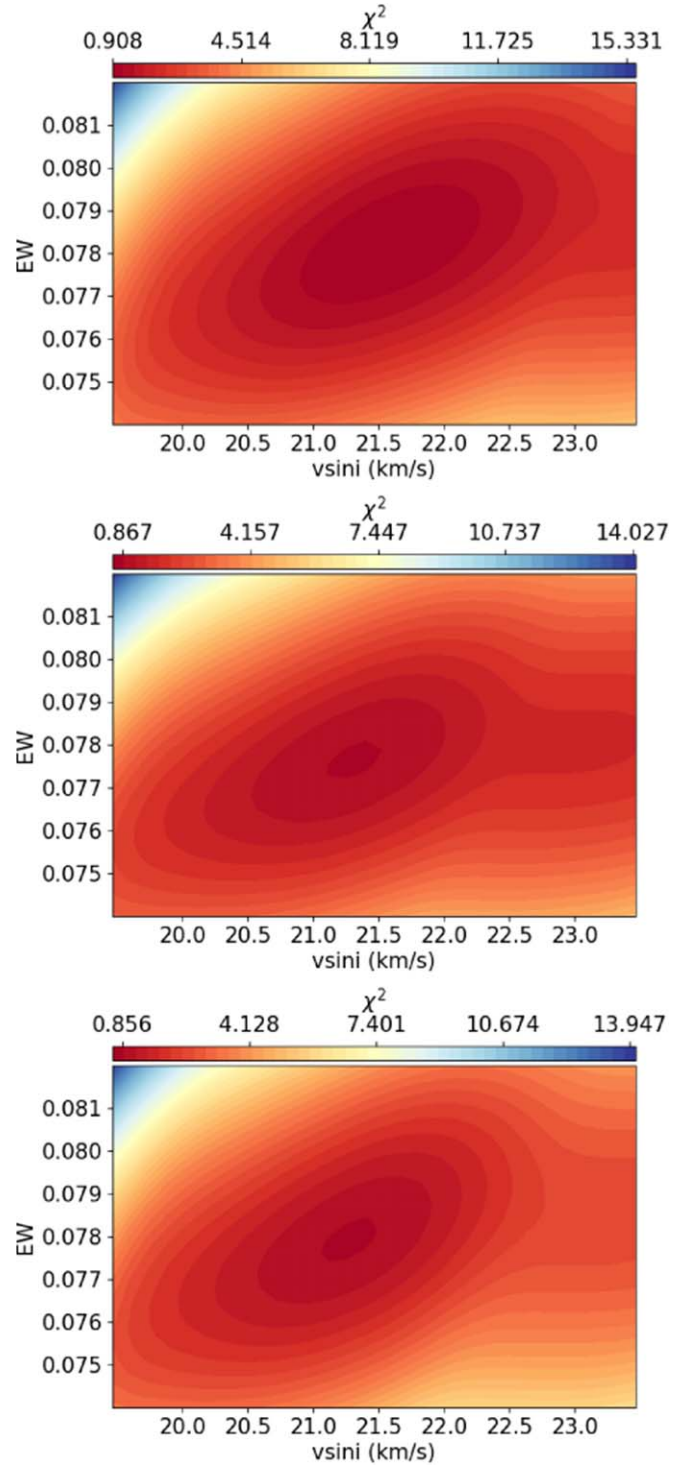


**Figure 4.** 2D grid search on the EW– $v \sin i$  plane for Set 1 (top), Set 2 (middle), and Set 3 (bottom). The colors show the  $\chi^2$  values.

intensity factors due to the gravity-darkening effect are determined, considering the study by Espinosa Lara & Rieutord (2011). SpotDIPy offers two options for surface grid generation: triangulation (supplied by PHOEBE2<sup>11</sup> Python package (Prša et al. 2016)), and trapezoidal discretization based on trapezoidal elements.

SpotDIPy uses the maximum entropy method to solve the ill-posed inverse problem by taking a regularization function of

<sup>11</sup> [github.com/phoebe-project/phoebe2](https://github.com/phoebe-project/phoebe2)

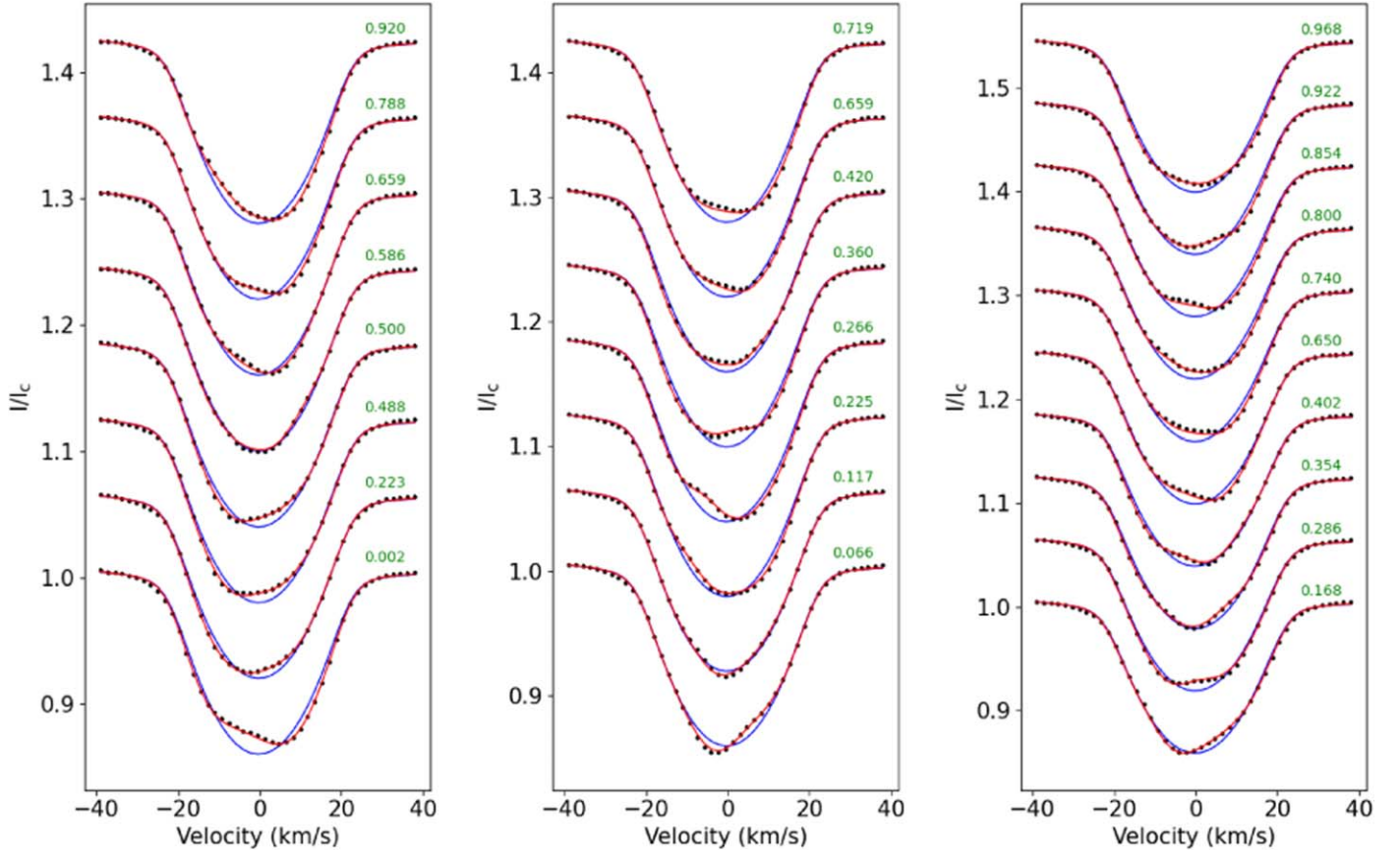


**Figure 5.** Phase-ordered LSD profiles (filled circles) with the error bars derived from the observed spectra, the spotless synthetic line profiles (blue solid lines), and the best-fit models (red solid lines) generated by the reconstruction process. The left, middle, and right panels are for Sets 1–3, respectively.

the form

$$S(f_s) = -\sum_{i=1}^n w_i \left[ f_{s_i} \log \frac{f_{s_i}}{m} + (1 - f_{s_i}) \log \frac{(1 - f_{s_i})}{(1 - m)} \right], \quad (2)$$

where  $w_i$  is the area of the  $i$ th surface element and  $m$  is the default minimum fraction of spot coverage that is set to a very small, positive value. To find the best-fitting spot distribution over the visible part of the stellar surface, we use the error function

$$E = \sum_{\phi} \sum_{\nu} \left[ \frac{R_{\text{calc}}(\nu, \phi) - R_{\text{obs}}(\nu, \phi)}{\sigma_{\nu, \phi}} \right]^2 + \lambda S, \quad (3)$$

where  $R_{\text{calc}}$  and  $R_{\text{obs}}$  are the calculated and observed mean line profiles (as a function of radial velocity  $\nu$ ) at phase  $\phi$  with uncertainty  $\sigma$ , and  $\lambda$  is the Lagrange multiplier (see Collier Cameron 1992, for more details of DI based on the two-temperature model). SpotDIPy searches for the best Lagrange multiplier using the method suggested by Chiang et al. (2005), where the minimum  $\chi^2$  and the entropy are calculated for each Lagrange multiplier during the optimization process. Then, the Lagrange multiplier that corresponds to the maximum curvature of the function  $\chi^2$  of entropy is used during the DI reconstruction. SpotDIPy uses the L-BFGS-B algorithm (see Byrd et al. 1995; Zhu et al. 1997, for more details) to solve the bound-constrained optimization problem, which is available in the SciPy<sup>12</sup> library.

To test the robustness of SpotDIPy, we use DoTS as the comparison case, since the latter has been extensively used in the literature for DI purposes. In this context, using the DoTS code, we generated synthetic line profiles with an S/N value of 500, including five spots with different sizes and locations, to simulate a spotted single star. We also assumed three different axial inclinations as  $30^\circ$ ,  $60^\circ$ , and  $90^\circ$ . The synthetic line profiles were generated with a sampling interval of 0.1 in phase. The stellar parameters were adopted as  $v \sin i = 40 \text{ km s}^{-1}$ , mass =  $1 M_\odot$ , and period = 1.5 days. These profiles were then used as input data for the surface reconstruction process performed using both DoTS and SpotDIPy. The surface grids for both codes were generated using 90 latitudinal zones that correspond to 180 surface elements along the equator, which is above the lower limit (80 surface elements) for the adopted  $v \sin i$  value and the resolution ( $R = 150,000$ ). Optimization was carried out until the same  $\chi^2$  value was obtained in both codes as  $\sim 1$ . Consequently, we calculated the standard deviations of the residuals, differences between models obtained from DoTS and SpotDIPy, in the order of  $4.8 \times 10^{-4}$ ,  $3.9 \times 10^{-4}$ , and  $3.4 \times 10^{-4}$ , for the three different axial inclination cases. The resultant maps generated by SpotDIPy are quite similar to those of DoTS (see Appendix). Therefore, the test results showed that SpotDIPy can perform DI with the same accuracy as DoTS for single stars.

In addition to the automatic calculation of the limb- and gravity-darkening coefficients, SpotDIPy also takes into account the effects of macroturbulence and instrumental profile, unlike the DoTS code. SpotDIPy applies the macroturbulence broadening using the radial-tangential formulation adapted from SME

<sup>12</sup> <https://scipy.org/>

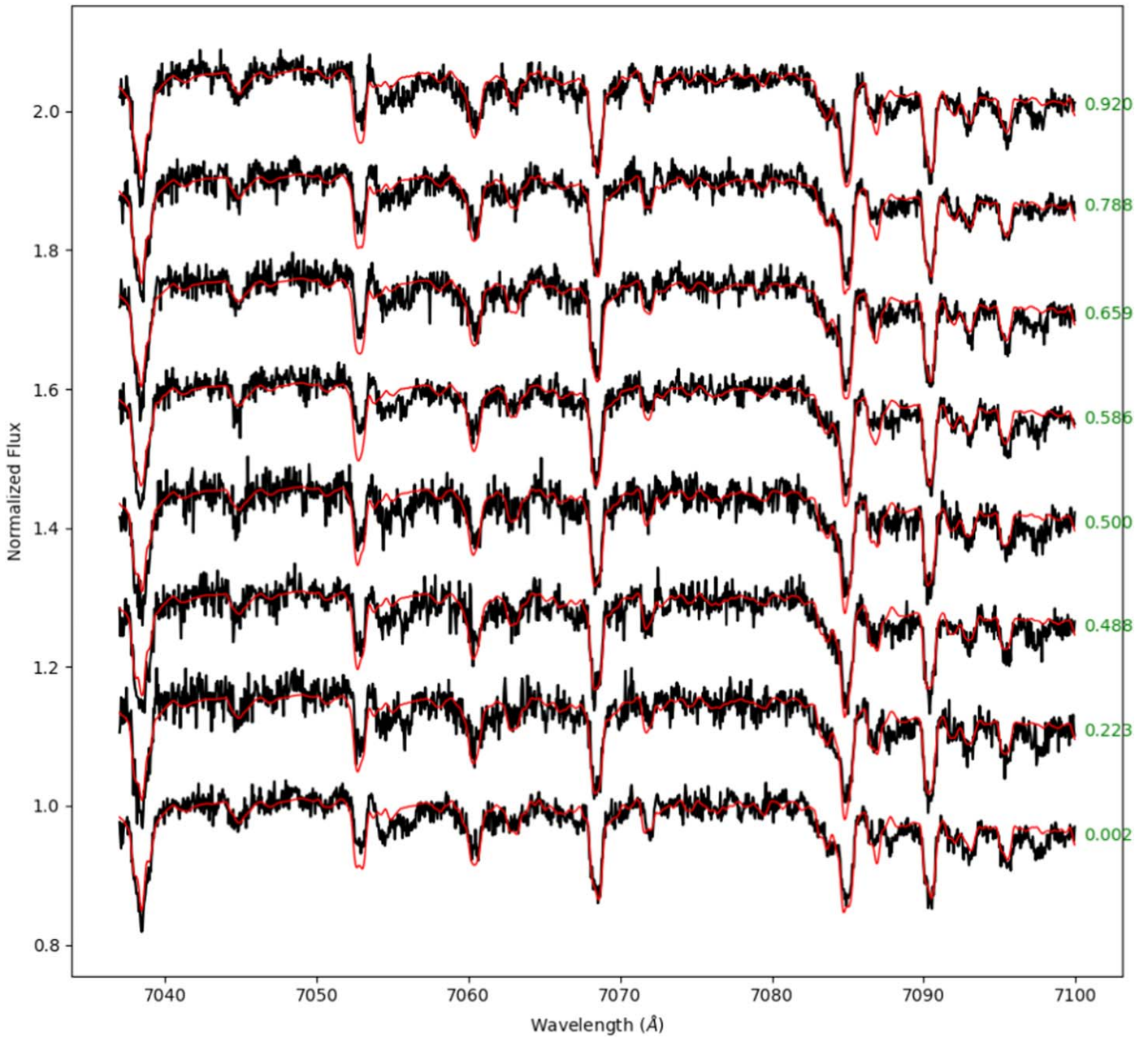


**Figure 6.** Phase-ordered TiO-band profiles (black solid lines) of Set 1 and the best-fit models (red solid lines) generated by the DI process.

(Valenti & Piskunov 1996). The instrumental profile is taken into account by convolving a kernel calculated over the given spectral resolution with the local line profiles, which is performed using the `PyAstronomy`<sup>13</sup> (Czesla et al. 2019) Python package.

Molecular bands, such as titanium oxide (TiO), play a crucial role in providing precise assessments of spot coverage on the surfaces of stars. The area covered by cool spots as a percentage of the total stellar surface area can be determined through the analysis of molecular bands (Berdyugina 2002). In this context, We developed `SpotDIPy` to reconstruct surface maps by simultaneously utilizing both atomic lines and molecular band profiles. The reconstruction process of TiO bands is the same as the DI process for atomic line profiles. The DI reconstruction process for TiO bands is identical to that for

atomic line profiles, with one notable distinction: in the TiO-band reconstruction process, the observed spectrum is directly matched with synthetic spectra determined by atmospheric parameters, representing the photosphere and spots without the need for an additional EW correction.

### 3.4. DI of PW And

We performed the DI of PW And and used `SpotDIPy` for Sets 1–3 separately. The surface grid was selected in trapezoidal discretization mode. Using Equation (9.1) of Kochukhov (2016), at least 12 resolution elements along the equator are sufficient to get a correctly reconstructed image for  $v \sin i = 21.4$  and  $R = 85,000$ . However, we used 90 latitudinal zones corresponding to a total of 12,406 surface elements, for better visualization. The local line profiles are generated using the synthetic spectra that are derived from the stellar parameters

<sup>13</sup> <https://github.com/sczesla/PyAstronomy>

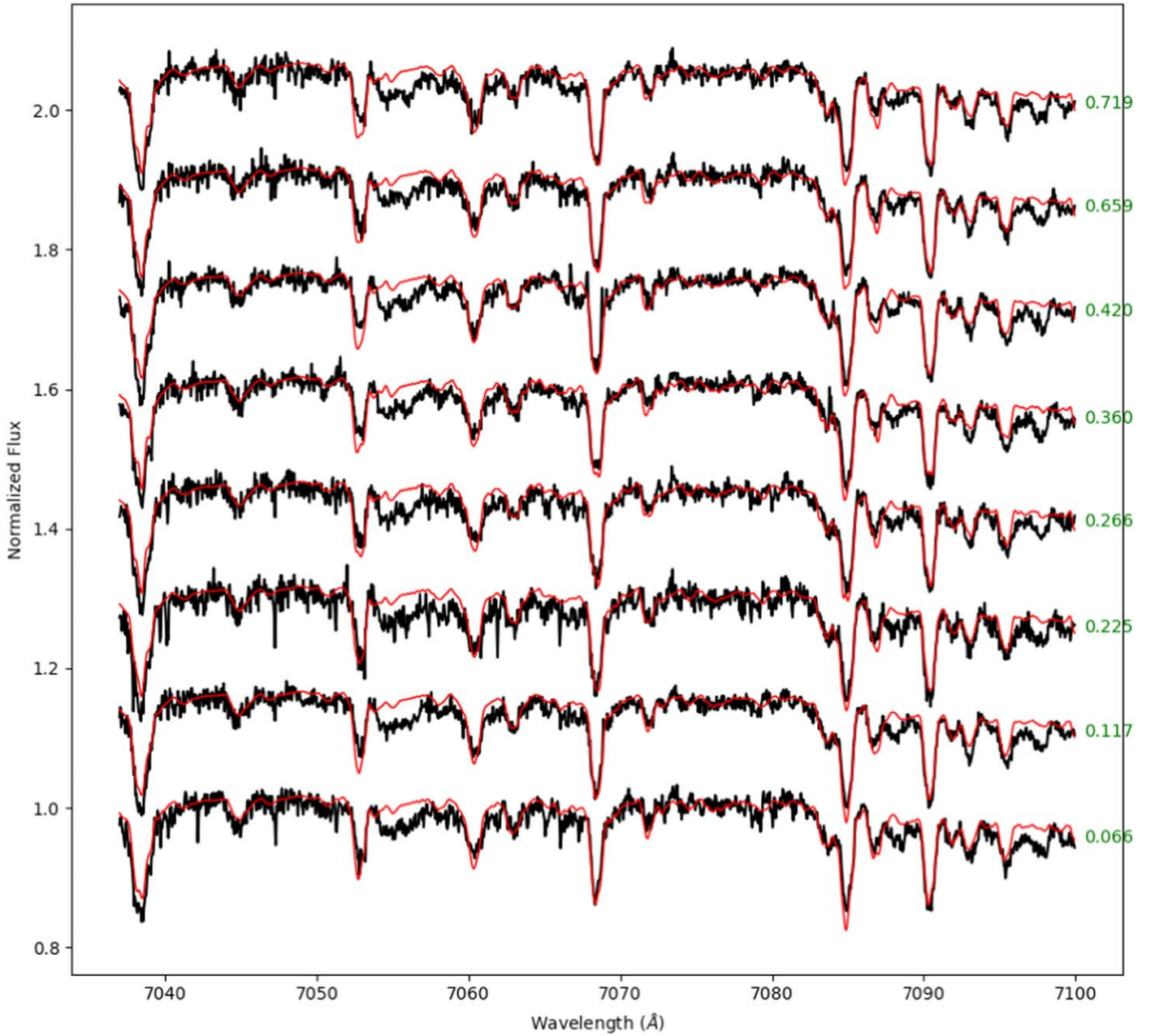


Figure 7. Same as Figure 6, but for Set 2.

provided in Table 2, which were employed to represent the quiet photosphere and spots, respectively. The same procedure was also applied to the TiO-band region (7000–7100 Å). Atomic and molecular line lists were extracted from VALD, while the synthetic spectra were generated using MARCS atmosphere models. We assumed the minimum spot temperature as 3800 K, which was given by Strassmeier & Rice (2006). The linear limb-darkening coefficients (Kostogryz et al. 2022, 2023) were determined according to the effective temperature, the surface gravity, and the metallicity of PW And. The gravity-darkening effect was also considered using Equation (31) of Espinosa Lara & Rieutord (2011). However, due to the relatively low equatorial rotational velocity of PW And, the gravity darkening has no significant effect on the observed profiles.

It is also possible to fine-tune the stellar parameters (e.g.,  $v \sin i$ ), using  $\chi^2$  minimization within SpotDIPy. As the

preliminary stellar parameters for DI, we used those given in Table 2. SpotDIPy uses an additional EW parameter, which affects the widths and depths of the local line profiles generated using synthetic spectra. EW thus allows us to control the depth of the LSD profiles, which are also critical to circumventing DI artifacts, such as spurious polar spots (Collier Cameron & Unruh 1994). To optimize EW, we carried out a two-dimensional grid search on the EW– $v \sin i$  plane, using the  $\chi^2$  minimization feature of SpotDIPy, where the algorithm searches for a minimum  $\chi^2$  for a particular value of the Lagrange multiplier, for each pair of EW– $v \sin i$  parameters. Contour plots of the resulting  $\chi^2$  for three sets are shown in Figure 4. The minimum  $\chi^2$  values turned out to be at  $v \sin i = 21.5^{+1.4}_{-1.3}$  km s<sup>−1</sup> for Set 1,  $21.3^{+2.2}_{-1.5}$  km s<sup>−1</sup> for Set 2, and  $21.3^{+1.1}_{-1.3}$  km s<sup>−1</sup> for Set 3. The errors of the  $v \sin i$  parameters were estimated from  $\chi^2_{\min} + 1$  of  $v \sin i$  values obtained from a 2D grid search (see

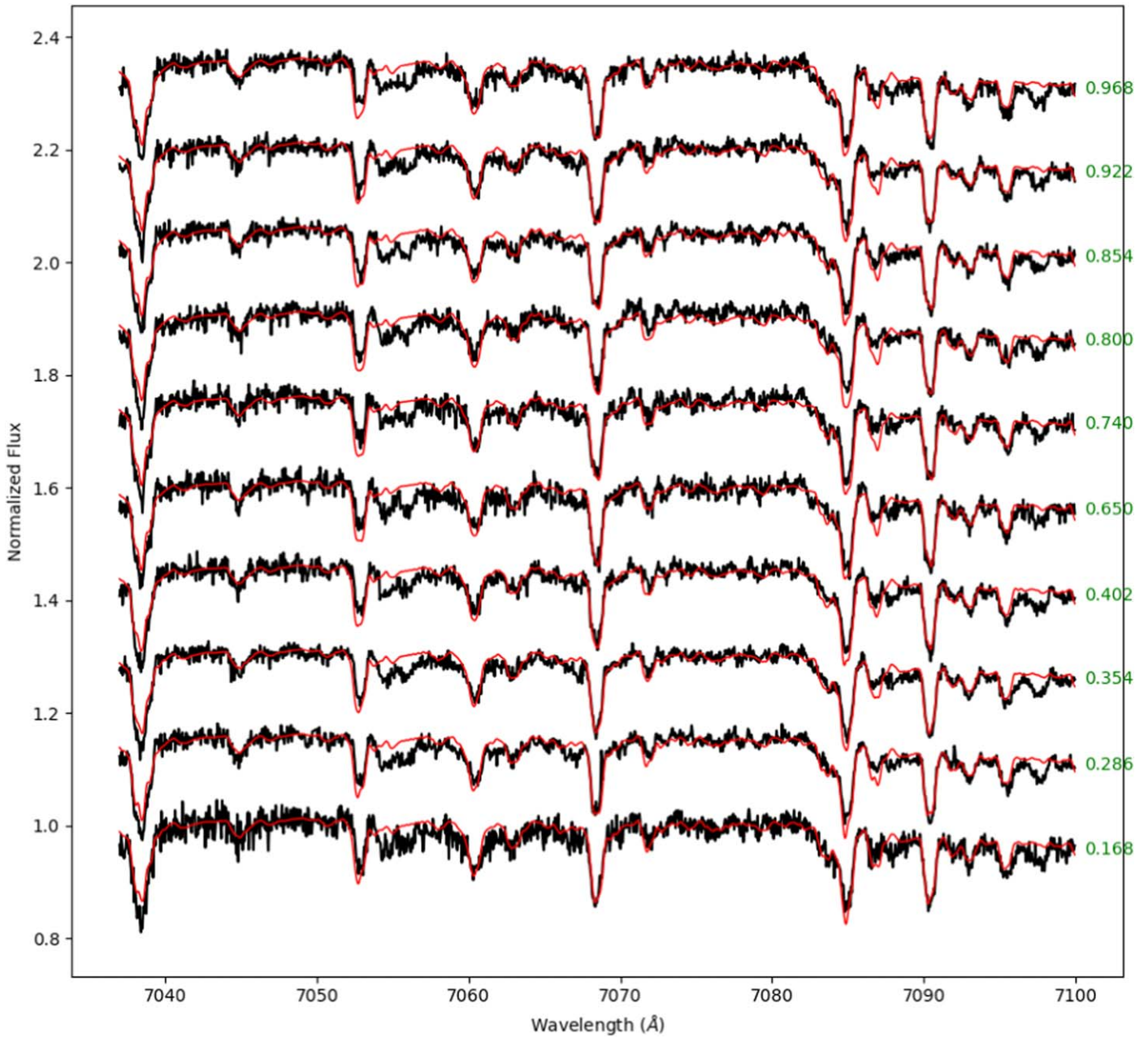


Figure 8. Same as Figure 6, but for Set 3.

Bevington & Robinson 2003, for more details). The average  $v \sin i$  was calculated as  $21.4^{+1.0}_{-0.8} \text{ km s}^{-1}$ , which is slightly lower than the one determined by Strassmeier & Rice (2006) and almost the same as found by Llorente de Andrés et al. (2021). The adopted stellar parameters used in DI are listed in Table 2. The LSD profiles, TiO-band profiles, and their respective best-fit models for all data sets are illustrated in Figure 5 and Figures 6–8, respectively. It is evident from Figure 5 and Figures 6–8 that the models obtained through DI are highly compatible with both LSD and TiO molecular band profiles. The Mollweide projections of the resulting DI maps for Sets 1–3 are shown in Figure 9.

The map of Set 1 shows a high-latitude spot region centered at about a latitude of  $75^\circ$  and midlatitude spots distributed around  $30^\circ$  latitude. Sets 2 and 3 show similar latitudinal distributions as can be seen in the map of Set 1, with a predominant high-latitude spot and other spots spread over

midlatitudes, particularly around  $30^\circ$  latitude. Although there is almost a 3 yr time span between Set 1 and Sets 2 and 3, the longitudinal distributions of starspots also show similarities, with the exception of a jump in longitude of the high-latitude spot from 2015–2018. The same feature is found roughly at the same longitude but with a different size when comparing the Set 2 and Set 3 maps.

The latitudinal distributions we found for all sets of maps are clearly different from the surface map obtained by Strassmeier & Rice (2006), which showed dominated low-latitude spots between  $+40^\circ$  and  $-20^\circ$ . A similar result was obtained by Kolbin & Galeev (2017), who found spots covering latitudes from  $30^\circ$ – $60^\circ$ . The surface maps obtained by Gu et al. (2010), on the other hand, exhibited a very large high-latitude spot, which extends to intermediate latitudes, making it a much more similar pattern to those in Figure 9.

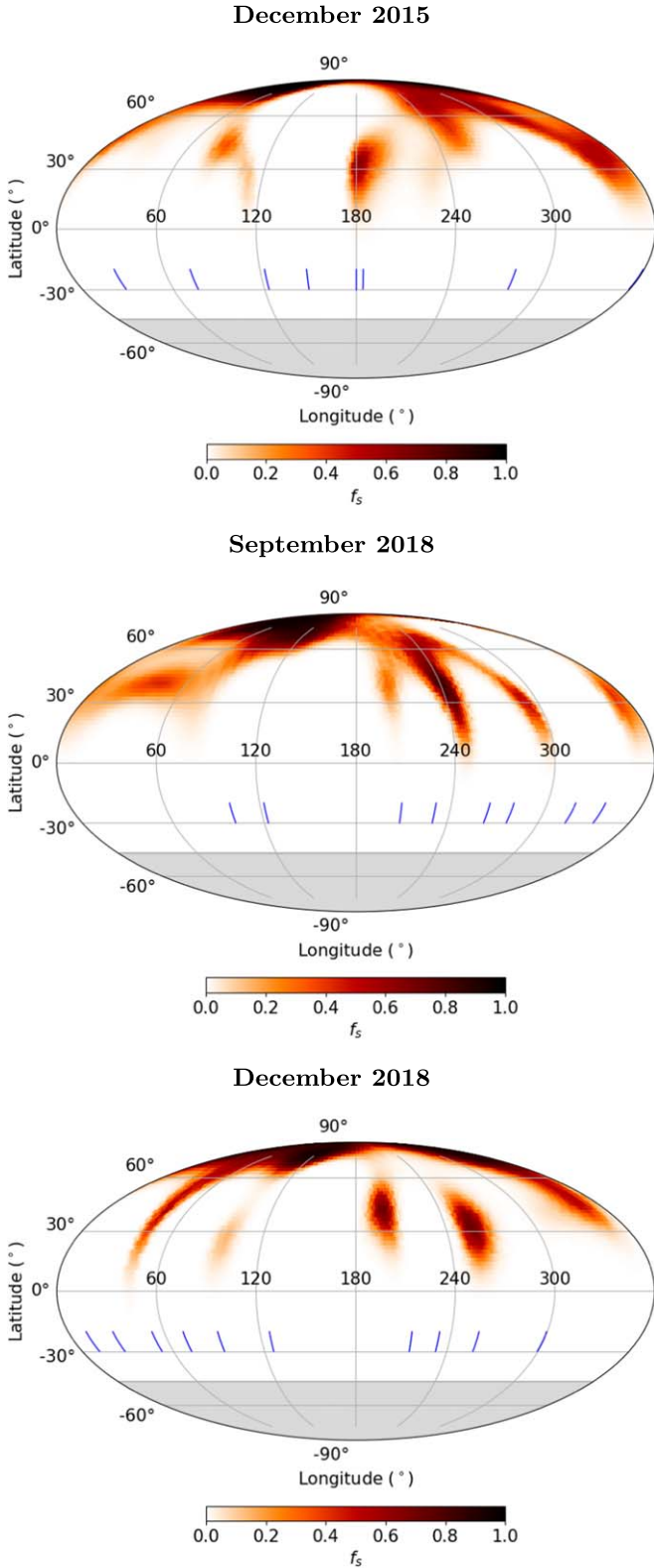


**Figure 9.** Mollweide projections of the reconstructed maps of PW And in terms of spot-filling factors. The first three panels from top to bottom show a map of Sets 1–3, respectively. The tick marks in the Mollweide projection show the phase coverage of spectral data. The shaded region around the south pole of the projection indicates the unseen region of PW And’s surface, due to the axial inclination.

The number of rotational cycles included in the spectroscopic data is a crucial factor to consider when generating DI maps. This is especially important when accounting for short-term

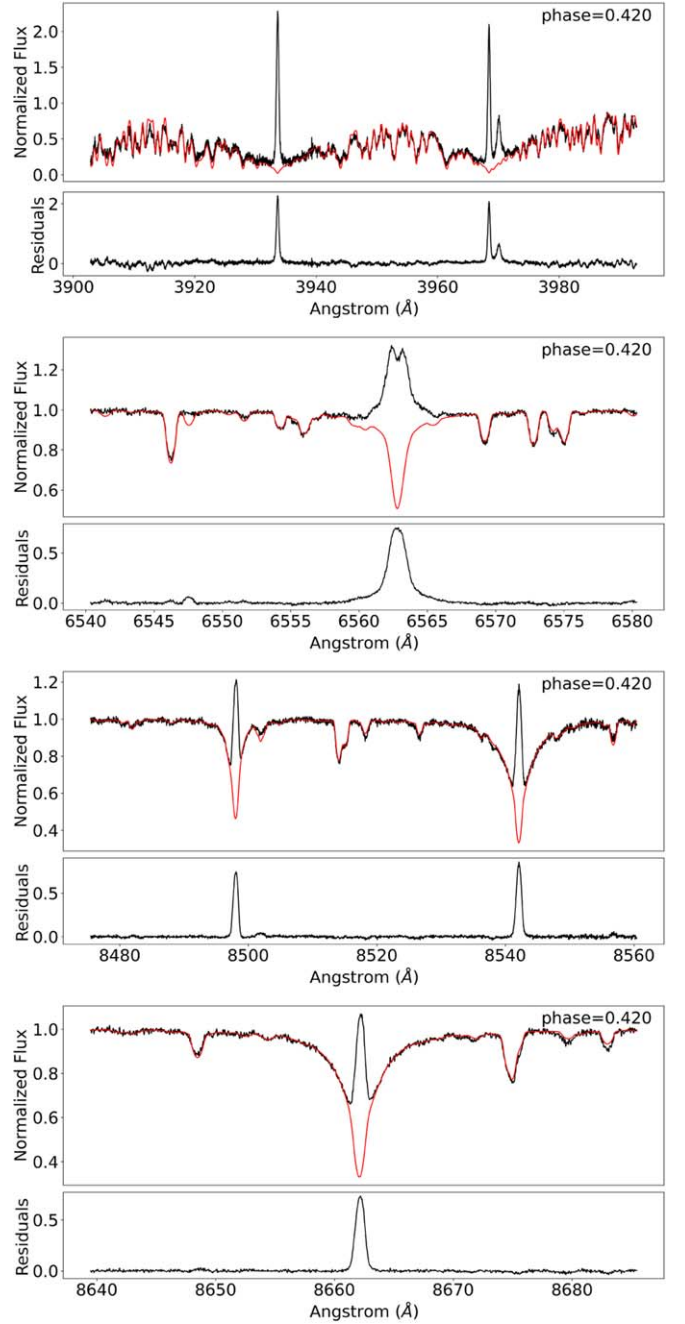


**Figure 10.** An example of spectral subtraction of Ca II H&K,  $H_{\alpha}$ , and Ca II IRT lines at the rotational phase 0.413 in Set 2. The red solid lines show the synthesized spectrum of HD 166620. The black solid lines above and below show the observed and subtracted spectra in each panel, respectively.

magnetic evolution and/or a high differential rotation rate, as it can influence the presence of artificial features in the resulting maps. In the study conducted by Gu et al. (2010), the maps were reconstructed using spectroscopic data that covered approximately 13.7 and 8.6 rotational cycles for subset 1 and subset 2, respectively. It is essential to acknowledge that reconstructed maps may exhibit artifacts due to the inclusion of spectroscopic data with relatively high rotation cycles. On the other hand, Strassmeier & Rice (2006) and Kolbin & Galeev (2017) utilized spectroscopic data encompassing approximately 3.4 and 4.6 rotation cycles, respectively. Considering the Set 1, Set 2, and Set 3 data used in this study, these values decrease to 2.9, 2.4,

**Table 3**  
Measurements of EEQWs of Ca II H&K, H $\alpha$ , and Ca II IRT

| BJD <sub>Mid</sub> | Ca II             |                   | H $\alpha$        | Ca II IRT         |                   |                   |
|--------------------|-------------------|-------------------|-------------------|-------------------|-------------------|-------------------|
|                    | K                 | H                 |                   | $\lambda$ 8498    | $\lambda$ 8542    | $\lambda$ 8662    |
| 57371.33485        | 0.866 $\pm$ 0.117 | 1.055 $\pm$ 0.126 | 1.249 $\pm$ 0.071 | 0.595 $\pm$ 0.060 | 0.775 $\pm$ 0.039 | 0.627 $\pm$ 0.028 |
| 57372.32557        | 0.873 $\pm$ 0.101 | 1.050 $\pm$ 0.126 | 1.252 $\pm$ 0.083 | 0.515 $\pm$ 0.063 | 0.683 $\pm$ 0.038 | 0.563 $\pm$ 0.045 |
| 57373.31892        | 0.916 $\pm$ 0.131 | 0.943 $\pm$ 0.133 | 0.919 $\pm$ 0.063 | 0.458 $\pm$ 0.067 | 0.579 $\pm$ 0.040 | 0.488 $\pm$ 0.028 |
| 57375.30687        | 0.846 $\pm$ 0.062 | 1.023 $\pm$ 0.083 | 0.910 $\pm$ 0.070 | 0.461 $\pm$ 0.063 | 0.605 $\pm$ 0.035 | 0.493 $\pm$ 0.029 |
| 57375.45063        | 0.791 $\pm$ 0.122 | 1.072 $\pm$ 0.147 | 0.904 $\pm$ 0.075 | 0.481 $\pm$ 0.059 | 0.627 $\pm$ 0.036 | 0.507 $\pm$ 0.023 |
| 57376.30420        | 0.873 $\pm$ 0.085 | 1.115 $\pm$ 0.098 | 1.127 $\pm$ 0.081 | 0.501 $\pm$ 0.059 | 0.613 $\pm$ 0.049 | 0.524 $\pm$ 0.043 |
| 57376.32586        | 0.864 $\pm$ 0.162 | 1.049 $\pm$ 0.165 | 1.130 $\pm$ 0.078 | 0.478 $\pm$ 0.052 | 0.633 $\pm$ 0.050 | 0.519 $\pm$ 0.035 |
| 57376.47667        | 0.759 $\pm$ 0.062 | 0.991 $\pm$ 0.094 | 1.006 $\pm$ 0.068 | 0.456 $\pm$ 0.063 | 0.591 $\pm$ 0.038 | 0.491 $\pm$ 0.027 |
| 58387.36672        | 1.009 $\pm$ 0.094 | 1.135 $\pm$ 0.115 | 0.678 $\pm$ 0.069 | 0.399 $\pm$ 0.059 | 0.560 $\pm$ 0.037 | 0.444 $\pm$ 0.023 |
| 58387.45742        | 0.963 $\pm$ 0.086 | 1.248 $\pm$ 0.141 | 0.765 $\pm$ 0.065 | 0.412 $\pm$ 0.061 | 0.552 $\pm$ 0.033 | 0.442 $\pm$ 0.024 |
| 58388.40970        | 0.854 $\pm$ 0.124 | 1.063 $\pm$ 0.121 | 0.637 $\pm$ 0.060 | 0.410 $\pm$ 0.059 | 0.558 $\pm$ 0.039 | 0.445 $\pm$ 0.021 |
| 58388.51470        | 1.193 $\pm$ 0.104 | 1.479 $\pm$ 0.125 | 0.772 $\pm$ 0.064 | 0.423 $\pm$ 0.057 | 0.564 $\pm$ 0.033 | 0.456 $\pm$ 0.023 |
| 58389.40298        | 0.832 $\pm$ 0.086 | 1.146 $\pm$ 0.119 | 0.788 $\pm$ 0.066 | 0.423 $\pm$ 0.062 | 0.567 $\pm$ 0.036 | 0.459 $\pm$ 0.028 |
| 58389.47599        | 0.909 $\pm$ 0.096 | 1.142 $\pm$ 0.129 | 0.789 $\pm$ 0.071 | 0.405 $\pm$ 0.063 | 0.567 $\pm$ 0.030 | 0.465 $\pm$ 0.025 |
| 58391.39727        | 0.811 $\pm$ 0.053 | 1.060 $\pm$ 0.085 | 0.904 $\pm$ 0.062 | 0.442 $\pm$ 0.061 | 0.595 $\pm$ 0.031 | 0.469 $\pm$ 0.027 |
| 58391.50205        | 0.841 $\pm$ 0.054 | 1.057 $\pm$ 0.090 | 1.530 $\pm$ 0.050 | 0.658 $\pm$ 0.056 | 0.836 $\pm$ 0.030 | 0.706 $\pm$ 0.016 |
| 58467.44046        | 0.936 $\pm$ 0.113 | 1.168 $\pm$ 0.151 | 0.706 $\pm$ 0.071 | 0.446 $\pm$ 0.063 | 0.601 $\pm$ 0.034 | 0.495 $\pm$ 0.028 |
| 58468.35045        | 0.946 $\pm$ 0.159 | 1.134 $\pm$ 0.148 | 1.097 $\pm$ 0.085 | 0.445 $\pm$ 0.075 | 0.586 $\pm$ 0.046 | 0.471 $\pm$ 0.045 |
| 58469.35515        | 0.801 $\pm$ 0.100 | 1.107 $\pm$ 0.140 | 0.740 $\pm$ 0.072 | 0.415 $\pm$ 0.056 | 0.566 $\pm$ 0.030 | 0.470 $\pm$ 0.025 |
| 58469.46048        | 0.799 $\pm$ 0.077 | 1.025 $\pm$ 0.096 | 0.831 $\pm$ 0.075 | 0.432 $\pm$ 0.061 | 0.585 $\pm$ 0.039 | 0.472 $\pm$ 0.020 |
| 58470.31374        | 1.375 $\pm$ 0.056 | 1.880 $\pm$ 0.098 | 0.937 $\pm$ 0.070 | 0.438 $\pm$ 0.068 | 0.595 $\pm$ 0.042 | 0.481 $\pm$ 0.017 |
| 58470.43395        | 0.867 $\pm$ 0.069 | 1.135 $\pm$ 0.094 | 0.915 $\pm$ 0.061 | 0.425 $\pm$ 0.060 | 0.560 $\pm$ 0.044 | 0.467 $\pm$ 0.020 |
| 58470.51817        | 0.837 $\pm$ 0.048 | 1.171 $\pm$ 0.097 | 0.868 $\pm$ 0.062 | 0.419 $\pm$ 0.062 | 0.555 $\pm$ 0.034 | 0.444 $\pm$ 0.023 |
| 58471.31222        | 0.948 $\pm$ 0.158 | 1.064 $\pm$ 0.194 | 0.814 $\pm$ 0.071 | 0.426 $\pm$ 0.062 | 0.566 $\pm$ 0.035 | 0.469 $\pm$ 0.023 |
| 58471.43170        | 1.112 $\pm$ 0.166 | 1.208 $\pm$ 0.177 | 0.823 $\pm$ 0.072 | 0.401 $\pm$ 0.065 | 0.570 $\pm$ 0.034 | 0.434 $\pm$ 0.021 |
| 58471.51305        | 0.953 $\pm$ 0.162 | 1.055 $\pm$ 0.167 | 0.874 $\pm$ 0.063 | 0.426 $\pm$ 0.063 | 0.578 $\pm$ 0.036 | 0.466 $\pm$ 0.022 |

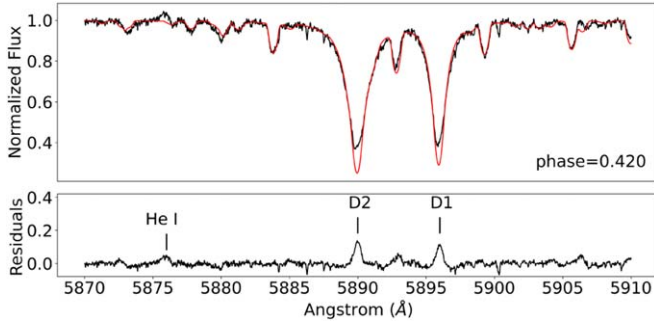


**Figure 11.** Excess emissions of He I D<sub>3</sub>, Na I (D<sub>1</sub>, D<sub>2</sub>) lines at phase 0.413 of Set 2.

and 2.3, respectively. Such a lower number of rotational cycles are more conducive to DI, as they reduce the likelihood of significant artificial features being introduced into the maps.

### 3.5. Chromospheric Activity Indicators

The presence of chromospheric activity on PW And has been known since the work by Bidelman (1985), who confirmed the existence of moderate emission in Ca II H&K lines. One of the most detailed investigations of the chromospheric activity of PW And was carried out by López-Santiago et al. (2003), who used all chromospheric indicator lines in the optical range by employing the spectral subtraction technique and mentioned that Balmer lines are clearly visible in emission in the subtracted spectra. Depending on the ratio of  $EW(H_{\alpha})$  and  $EW(H_{\beta})$  López-Santiago et al. (2003)

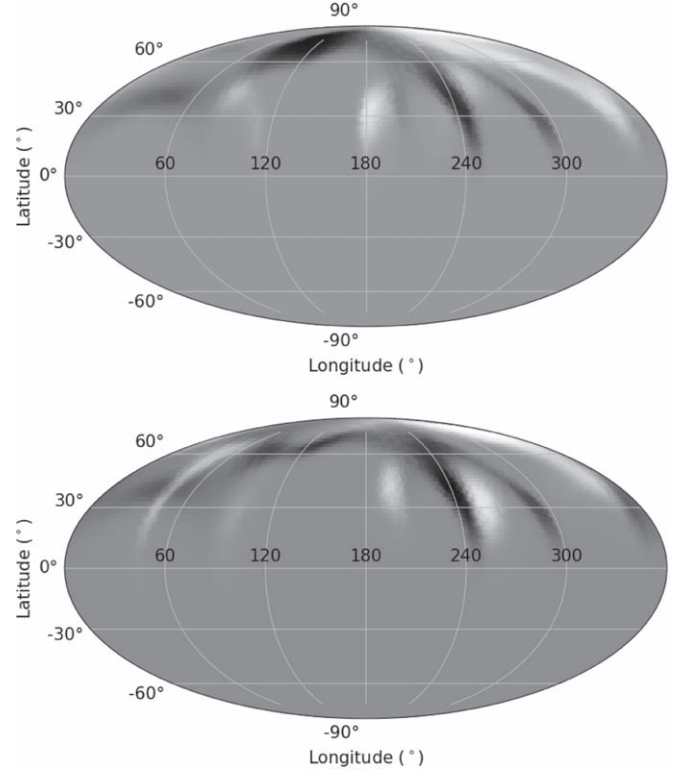


**Figure 12.** Comparison of the maps reconstructed using Sets 1–3. In both panels, black indicates the predominance of spot regions from Set 2. White indicates the predominance of spot regions from Set 1 and Set 3 in the upper and lower panels, respectively.

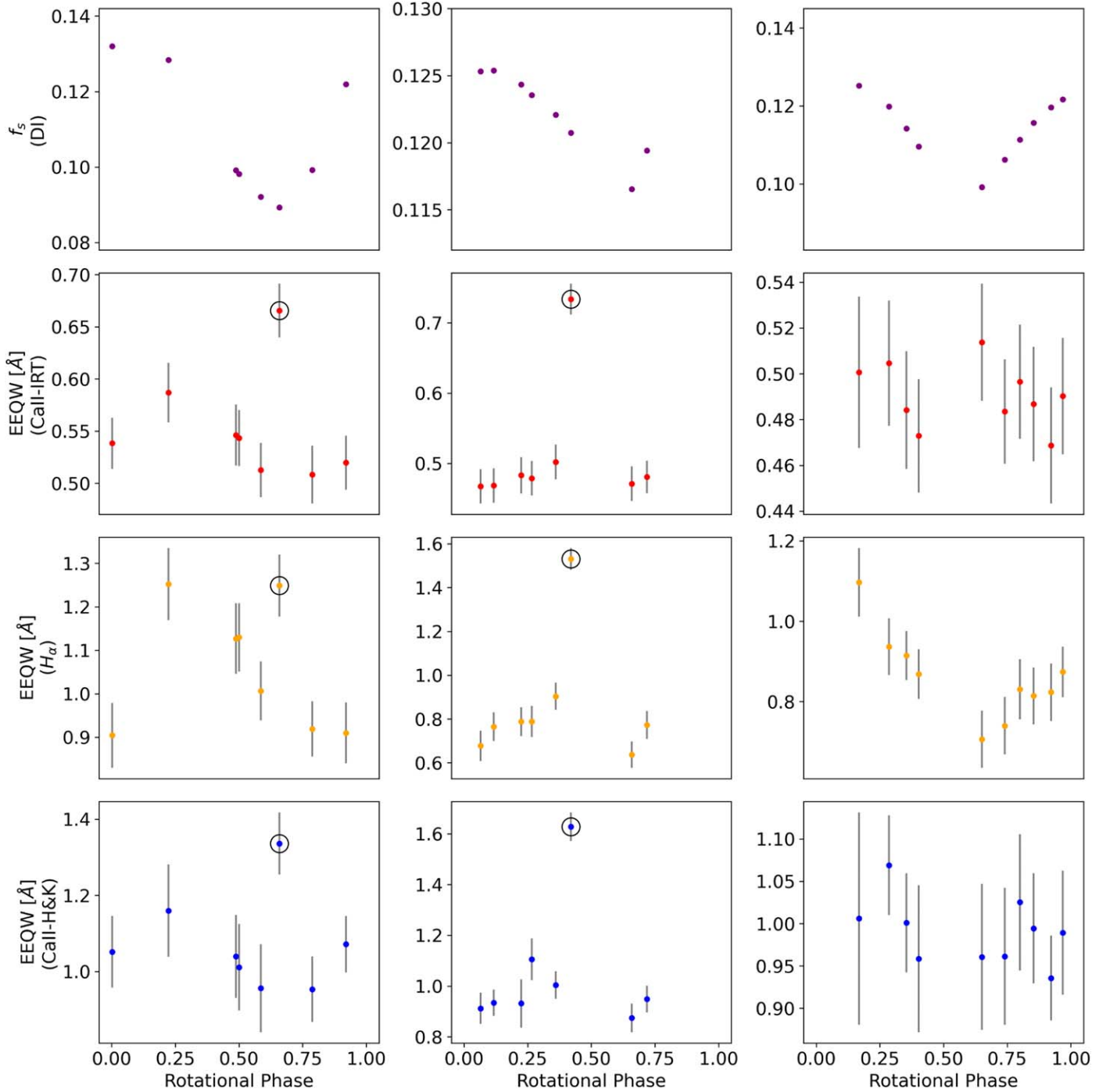


**Figure 13.** Comparison of photospheric and chromospheric activity-induced rotational modulations. The first row shows photospheric rotational modulations that arise from cool spots obtained from DI. The third row shows EEQW variations of  $H_{\alpha}$  lines, while the second and fourth rows show averaged EEQW variations of the Ca II IRT and Ca II H&K lines, respectively. From the left to the right, each column represents Sets 1–3 data, respectively. Large open circles denote flare events.

argued that the emission of these lines could arise from prominence-like material, whereas the ratio of the excess emission of two Ca II lines (8498 and 8542 Å) arise from plage-like regions. Employing the spectral subtraction technique to  $H_{\alpha}$  and Ca II IRT lines, Zhang et al. (2015) obtained similar findings concerning the strong magnetic activity of PW And.

Following the chromospheric activity results in the literature, we investigate the rotational modulation of PW And’s chromospheric excess emission, by applying the same method, spectral subtraction, for the Ca II H&K,  $H_{\alpha}$ , and Ca II IRT lines. By *excess*

*emission*, we hereafter mean the line emission left when the adapted synthetic spectrum obtained using the same stellar parameters of PW And was subtracted. We artificially broadened its spectral lines to the  $v \sin i$  value of PW And, 21.4 km s<sup>−1</sup>. We then subtracted the resulting continuum-normalized spectrum from each PW And spectrum. Comparisons of PW And Ca II H&K,  $H_{\alpha}$ , and Ca II IRT spectra with those from the synthetic spectrum are shown in Figure 10. Next, we measured the excess equivalent width (EEQW) in the Ca II H&K ( $\lambda 3968$  and  $\lambda 3933$ ),  $H_{\alpha}$  ( $\lambda 6563$ ), and Ca II IRT lines ( $\lambda 8498$ ,  $\lambda 8542$ , and  $\lambda 8662$ ) of

the subtracted spectra, by integrating over above the zero level of the subtracted profiles. We estimated the uncertainties of the EEQWs, using Equation (2.3) of Schöfer (2021). All EEQW measurements are listed in Table 3. The EEQW variations of Ca II H&K,  $H_{\alpha}$ , and Ca II IRT emissions along with the rotational phase for each data set that are shown in Figure 13 show similar trends among themselves. In Set 1, there is an abrupt increase in the EEQWs of all chromospheric emissions, observed during phase 0.659. A very similar phenomenon is evident for phase 0.420 of Set 2, for which the emission peaks also have distinctly higher values compared to the general trend. As a rapidly rotating K2 V star, PW And is expected to have strong flare activity. Two such flares were detected by López-Santiago et al. (2003), who were able to observe the entire pre-flare, flare, and gradual decay phases. To inspect a possible connection of abrupt increases in the EEQWs to flare activity, we measured the chromospheric flare diagnostic lines He I D<sub>3</sub> and the Na I doublet. Following spectral subtraction, we found them in excess emission, as can be seen in Figure 11. Therefore, we conclude that the two spectra that correspond to phases 0.659 and 0.420 of Set 1 and Set 2 data may be observed during pre-flare, flare, or gradual decay phases.

#### 4. Conclusion and Discussion

In this study, we analyzed high-resolution spectra of PW And considering three data sets obtained in different observing seasons, to investigate the activity nature of the star, using different methods. We also presented the most recent and accurate rotation period of PW And determined from the precise and almost continuous TESS light curves, by computing the Lomb–Scargle periodogram. The photospheric activity was investigated using the DI technique to reconstruct star-spot distributions. This was achieved by simultaneously modeling both the atomic line and TiO molecular band profile, utilizing a new Python-based DI code called *SpotDIPy*.

DI maps derived from Sets 1–3 data clearly show a dominant high-latitude spot as well as mid- to low-latitude spots down to  $\sim +30^\circ$  latitudes. It is remarkable that the high-latitude spot continues to exist, in spite of a 3 yr time span between Set 1 and Sets 2 and 3. The TESS light curves, also spanning 3 yr, exhibit almost the same light-curve characteristics as magnetic flux continuously emerges and decays within the same phase range over the entire time span, during which one longitude region is dominant (see Figure 2). López-Santiago et al. (2003) obtained the same finding using the CCF technique and mentioned that the variations of CCF bisectors found in three epochs reveal the prevalence over time of large spots or the existence of active longitudes where spots are continuously emerging. We compared the resulting surface maps of Sets 1–3 in Figure 12. It can be clearly seen that the high-latitude spot of Set 1 is located at lower longitudes than that of Set 2, while the high-latitude spots in Sets 2 and 3 were almost centered on the same longitude. Therefore, considering (a) the explanation by López-Santiago et al. (2003), (b) the TESS light curves, and (c) the DI maps presented in this study, the most plausible explanation for the main component of variability in PW And is the prevalence of large spots or spot groups over time. Moreover, this might indicate that differential rotation is minimal on PW And and future observations spanning more rotation cycles could be used to place firm limits on this.

We conducted some tests to investigate the impact of S/N and phase coverage on the maps obtained for PW And. In this context, an artificial map was created with the spot distribution seen in the top panel of Figure 17, and artificial line profiles were generated

based on the stellar parameters of PW And using this map. In the first test, we compared the maps obtained using line profiles having the same average S/N value and the phase coverage of Set 1, with the maps generated via the line profiles using the same S/N value but with a 0.05 phase interval. In the second test, unlike the first one, we compared the maps obtained from line profiles with significantly higher S/N values (Figure 17). As can be seen from the resultant maps, relatively low S/N and insufficient phase coverage provide lower spot coverage than expected. Additionally, depending on the axial inclination, spots near the unseen latitudes of the stellar surface tend to have latitudes higher than what is expected. Therefore, when considering S/N and phase coverage in PW And observations, it can be said that the total spot coverage may be underestimated to some extent and the latitudes of low-latitude spots may be somewhat overestimated.

The obtained spot distributions from DI are compatible with those of Gu et al. (2010). On the other hand, Strassmeier & Rice (2006) claimed that the spots on PW And are distributed between  $+40^\circ$  and  $-20^\circ$  latitude without the presence of a high-latitude spot. Gu et al. (2010), explained the reason for the large difference between the surface maps reconstructed by them and Strassmeier & Rice (2006) as the lifetime of the main spot structure cannot last more than one year and should change largely during its one activity cycle, similar to LQ Hya. Besides, a K0-type star’s convection zone has a larger fractional depth compared to that of a solar mass star. When combined with the strong Coriolis effect, this results in higher emergence latitudes and strong polar magnetic fields (Işık et al. 2011), which is in accordance with the spot distributions reconstructed for PW And in this study.

We show a comparison of DI-based  $f_s$  variations along with the chromospheric diagnostics for all sets in Figure 13. The EEQW variations of  $H_{\alpha}$ , Ca II H&K, and Ca II IRT emissions for the entire data set show almost the same trend among themselves. Besides, the flare event seen during Set 1 and Set 2 is clearly traceable from the abrupt increase in EEQWs of all indicator lines. It should be noted that there is almost 2.5 hr between phases 0.360 and 0.420, where the latter corresponds to a possible flare event. López-Santiago et al. (2003) mentioned that there are approximately 24 hr between the flare event and the pre-flare phase during their spectral observations of PW And. Therefore, the spectrum taken during phase 0.360 most likely corresponds to the pre-flare event.

The EEQW variation of the Ca II H&K, and Ca II IRT lines show very similar trends to DI  $f_s$  characteristics, while the variation of EEQWs for  $H_{\alpha}$  differs slightly. Compared to the  $f_s$  variations from DI, the chromospheric diagnostics show discrepancies due to the strong flare event in Set 2. The chromospheric excess emission variations are also in parallel with the  $f_s$  variations obtained from DI in Set 3, although the Ca II H&K, and Ca II IRT are more scattered. Our findings imply that PW And’s chromospheric activity patterns are spatially associated with its starspots.

Molecular bands, such as TiO bands, offer valuable insights into the examination of cool spots on the surfaces of active stars. However, achieving precise modeling of molecular bands particularly requires the consideration of the actual elemental abundances as well as the Doppler shifts to obtain a more accurate evaluation of spot coverage on stellar surfaces. In the study by Berdyugina (2002), synthetic TiO-band profiles generated from the spot distribution obtained through DI analysis of six atomic line profiles at 11 different rotational phases of IM Peg are seen to be in excellent agreement with the observed TiO-band profiles, proving that the recovered spot coverage from the atomic lines are reliable. In this study, a simultaneous DI process was employed to

effectively model both the atomic lines (LSD profiles) and the TiO-band profiles at 7055 Å of PW And (see Figures 5–8). The average S/N values obtained for atomic lines (LSDs) from Sets 1–3 are 732, 811, and 766, respectively, while for the TiO-band profiles, they are 86, 118, and 100. This implies that during inversion, atomic lines have 8.5, 6.9, and 7.7 times more weight compared to molecular band profiles. Therefore, it is clear that TiO bands exhibit significantly lower S/Ns compared to the LSD profiles, thereby giving the latter a more substantial weight on the resulting surface spot distributions in simultaneous DI processes. Nevertheless, the successful modeling of TiO bands performed in this study validates the accuracy of the spot distributions derived from these simultaneous analyses, as also achieved by Berdyugina (2002). Therefore, in order to precisely determine the spot characteristics, DI and TiO should be considered simultaneously.

We introduced a new Python-based DI code, SpotDIPy that is able to reconstruct the surface brightness distribution of single stars based on two-temperature model. SpotDIPy was tested with the help of some simulations in comparison with the well-known DI code DoTS. The test results showed that SpotDIPy gave almost identical maps as those obtained via DoTS in terms of reconstructing the surface brightness distribution of stars, indicating the success of the code SpotDIPy. SpotDIPy is an open-source code that allows other users to modify and develop it freely. It is user-friendly with certain plotting GUI capabilities and is simple to use. In the near future, we plan to adopt SpotDIPy for binary stars and also to provide a surface reconstruction option for the temperature distribution of stars. The code will be accessible on GitHub<sup>14</sup> by the end of 2023.

## Acknowledgments

We would like to thank the referee, Dr. Klaus Strassmeier, whose critical comments led to substantial improvement of the manuscript. H.V.Ş. acknowledges the support by The Scientific And Technological Research Council of Türkiye (TÜBİTAK) through project No. 1001-115F033. D.M. acknowledges financial support from the Agencia Estatal de Investigación of the Spanish Ministerio de Ciencia e Innovación through project No. PID2019-109522GB-C5[1:4]/AEI/10.13039/501100011033. O.K. acknowledges support from the Swedish Research Council (project No. 2019-03548).

*Software:* DoTS (Collier Cameron 1992), SpotDIPy (Bahar 2023), ExoTiC-LD (Grant & Wakeford 2022), PHOEBE2 (Prša et al. 2016), SciPy (Virtanen et al. 2020), PyAstronomy (Czesla et al. 2019), NumPy (Harris et al. 2020), Autograd (Maclaurin et al. 2015), Kneebow (Georg 2019), Astropy (Astropy Collaboration et al. 2013, 2018, 2022), PyQt (PyQT 2012), Matplotlib (Hunter 2007), Mayavi (Ramachandran & Varoquaux 2011).

## Appendix Test Results

We performed DI with both SpotDIPy and DoTS codes using the same spectral line profiles, and the resulting surface reconstructions are shown in Figures 14–16 (see Section 3.3 for details). Furthermore, Figure 17 presents a comparison of surface maps obtained through DI, considering spectral line profiles with different phase coverages and S/N values.

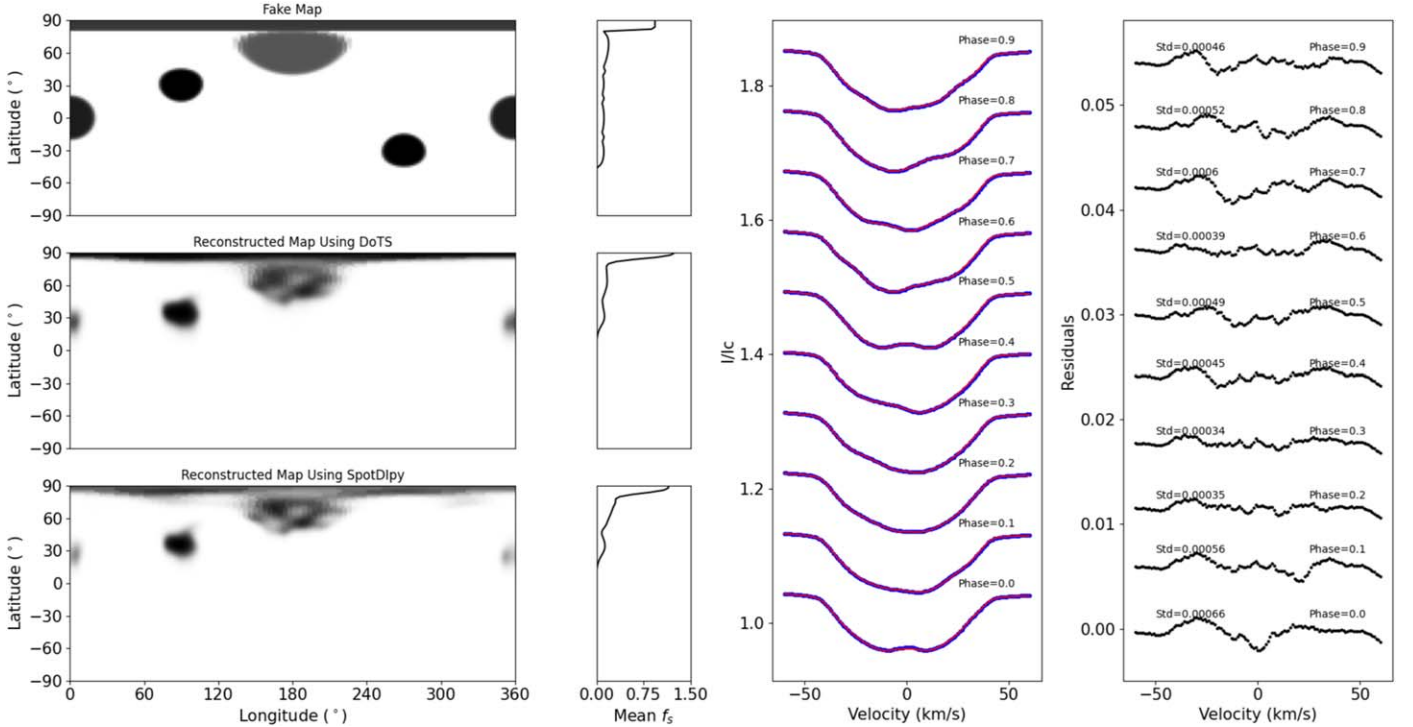


**Figure 14.** A comparison simulation of DoTS and SpotDIPy. In the first column, the original spotted map (top) and reconstructed maps using DoTS (middle) and SpotDIPy (bottom), respectively. The third column shows the latitudinal cross section of the spots recovered. The third column shows the best-fit models generated by DoTS (blue-filled circles) and SpotDIPy (red solid lines). Differences between the best-fit models with their standard deviations are shown in the fourth column. Phases correspond to each of the best fits and the residuals are indicated. Original spotted map and artificial synthetic line profiles with 500 S/Ns generated by DoTS under the 30° axial inclination.

<sup>14</sup> <https://github.com/EnginBahar/SpotDIPy>

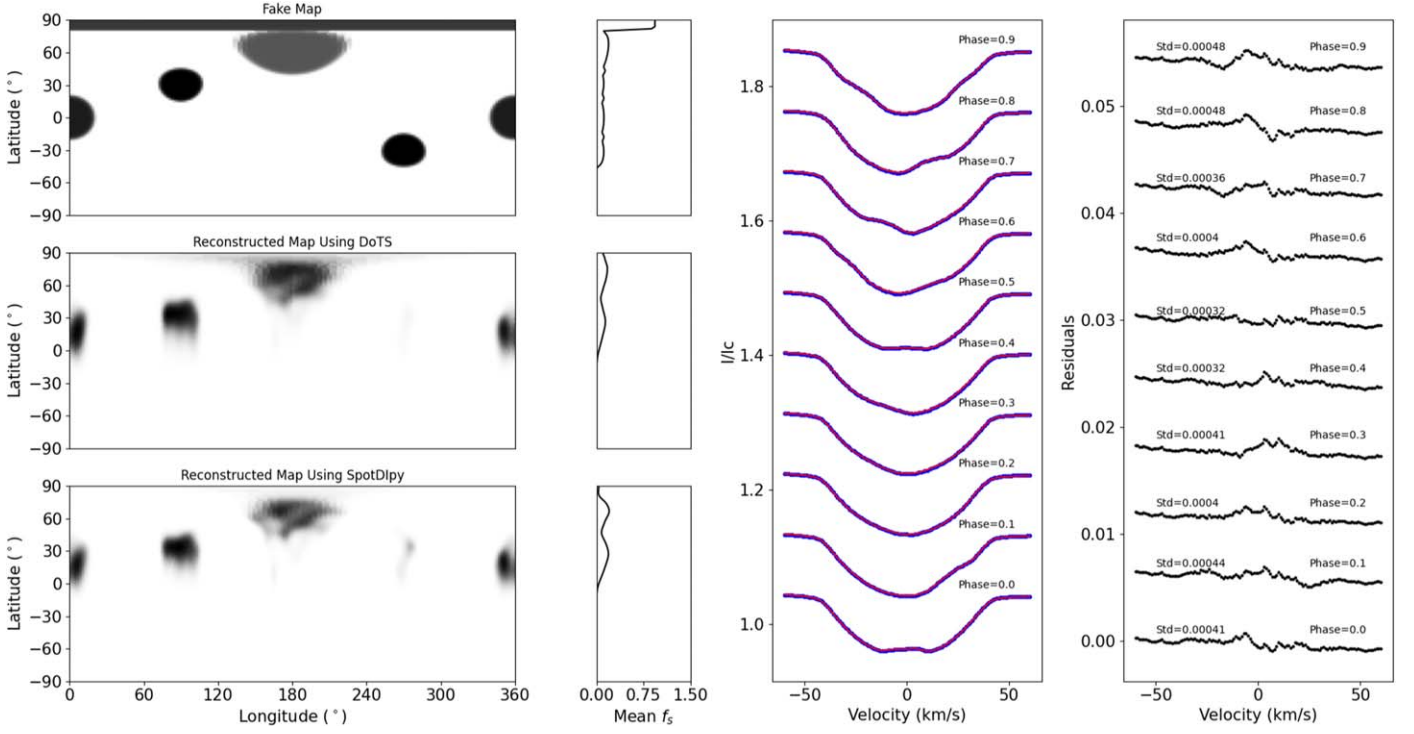


Figure 15. Same as Figure 14, but for 60° axial inclination.

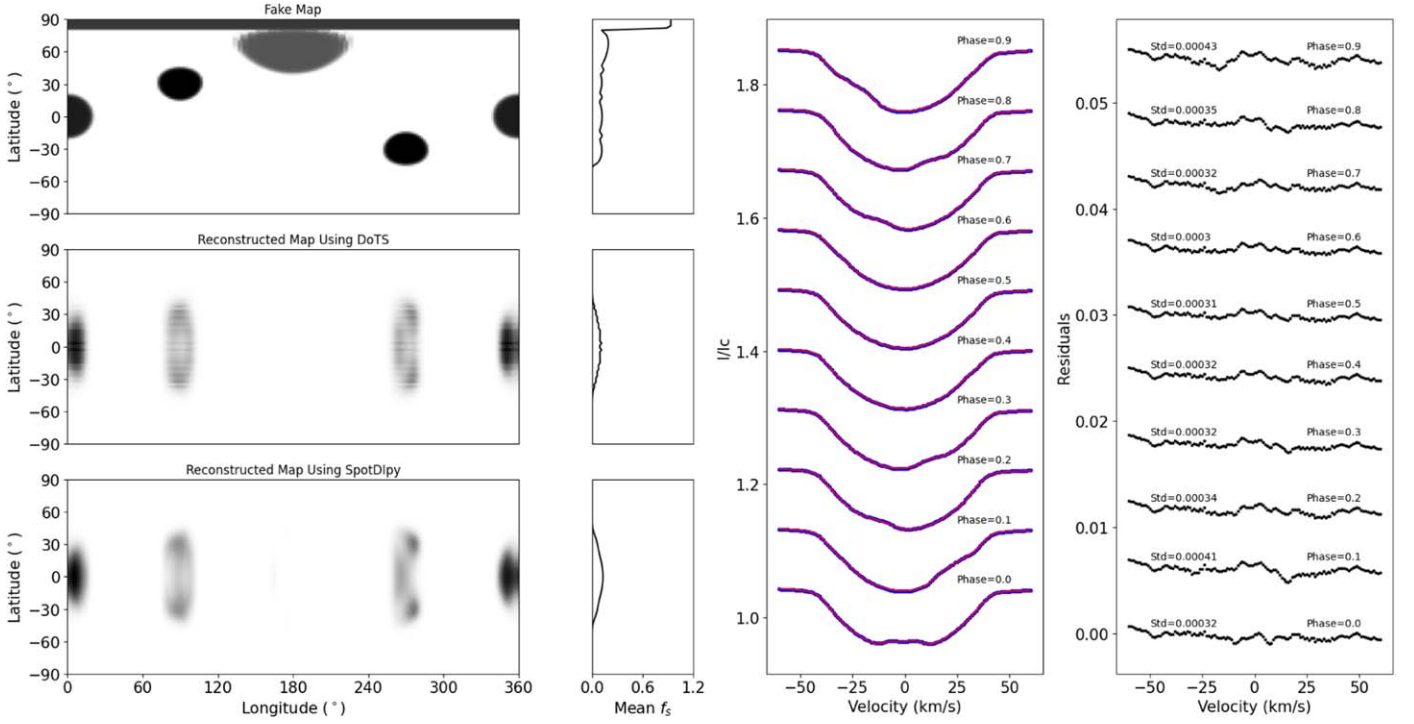
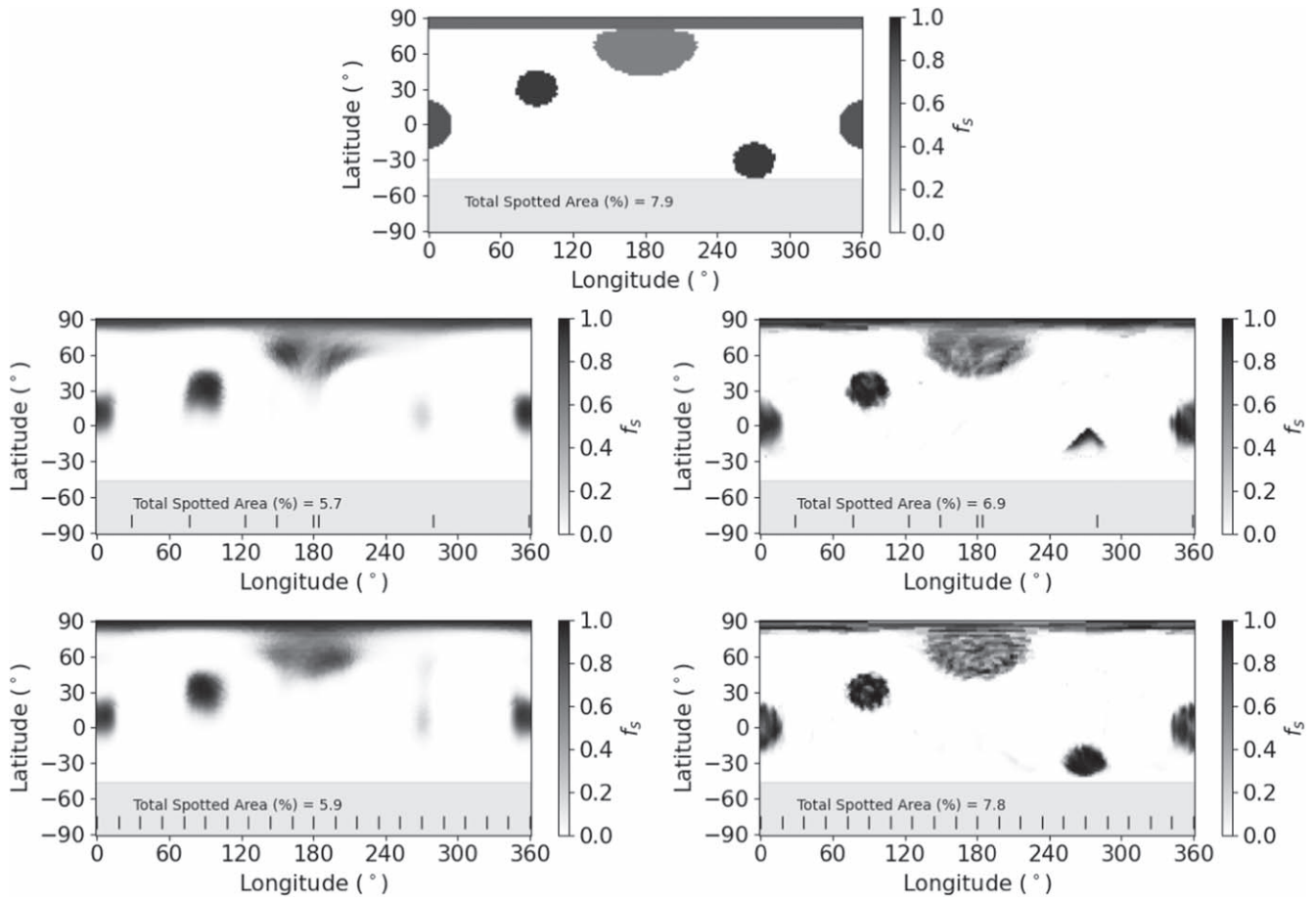


Figure 16. Same as Figure 14, but for 90° axial inclination.



**Figure 17.** Test results for the effect of S/N and phase coverage on the reconstructed surface images. The top map is an artificial map containing spots placed at different latitudes and longitudes, and all artificial line profiles have been generated from this map. The middle left image was reconstructed using line profiles with the same phase coverage and S/N as Set 1 data, while the lower left image used the same S/N but with a 0.05 phase sampling interval. In the middle right image, we maintained the same phase coverage but with a significantly higher S/N, while the lower right image combined a 0.05 phase sampling interval with a very high S/N. The shaded region around the south pole of the projection indicates the unseen region of the stellar surface.

### ORCID iDs

Engin Bahar <https://orcid.org/0000-0001-9119-2316>  
 Hakan V. Şenavcı <https://orcid.org/0000-0002-8961-277X>  
 Emre Işık <https://orcid.org/0000-0001-6163-0653>  
 Gaitee A. J. Hussain <https://orcid.org/0000-0003-3547-3783>  
 Oleg Kochukhov <https://orcid.org/0000-0003-3061-4591>  
 David Montes <https://orcid.org/0000-0002-7779-238X>  
 Yue Xiang <https://orcid.org/0000-0001-6580-9378>

### References

- Astropy Collaboration, Price-Whelan, A. M., Lim, P. L., et al. 2022, *ApJ*, **935**, 167
- Astropy Collaboration, Price-Whelan, A. M., Sipőcz, B. M., et al. 2018, *AJ*, **156**, 123
- Astropy Collaboration, Robitaille, T. P., Tollerud, E. J., et al. 2013, *A&A*, **558**, A33
- Berdugina, S. V. 2002, *AN*, **323**, 192
- Bahar, E. 2023, SpotDIPy, v0.0.4-alpha, Zenodo, doi:10.5281/zenodo.8386064
- Bevington, P. R., & Robinson, D. K. 2003, in *Data Reduction and Error Analysis for the Physical Sciences*, ed. S. J. Cotkin (New York: McGraw-Hill)
- Bidelman, W. P. 1985, *AJ*, **90**, 341
- Blanco-Cuaresma, S. 2019, *MNRAS*, **486**, 2075
- Blanco-Cuaresma, S., Soubiran, C., Heiter, U., & Jofré, P. 2014, *A&A*, **569**, A111
- Byrd, R. H., Lu, P., Nocedal, J., & Zhu, C. 1995, *JJSC*, **16**, 1190
- Chiang, Y.-W., Borbat, P. P., & Freed, J. H. 2005, *JMagR*, **177**, 184
- Collier Cameron, A. 1992, in *Surface Inhomogeneities on Late-Type Stars*, ed. P. B. Byrne & D. J. Mullan, Vol. 397 (Berlin: Springer), 33
- Collier Cameron, A., & Unruh, Y. C. 1994, *MNRAS*, **269**, 814
- Czesla, S., Schröter, S., Schneider, C. P., et al. 2019, PyA: Python astronomy-related packages, Astrophysics Source Code Library, ascl:1906.010
- Dempsey, R. C., Bopp, B. W., Strassmeier, K. G., et al. 1992, *ApJ*, **392**, 187
- Donati, J.-F., Semel, M., Carter, B. D., Rees, D. E., & Collier Cameron, A. 1997, *MNRAS*, **291**, 658
- Espinosa Lara, F., & Rieutord, M. 2011, *A&A*, **533**, A43
- Folsom, C. P., Petit, P., Bouvier, J., et al. 2016, *MNRAS*, **457**, 580
- Georg, U., 2019 kneebow: Knee or elbow detection for curves, <https://github.com/georg-un/kneebow>
- Grant, D., & Wakeford, H. R. 2022, Exo-TiC/ExoTiC-LD: ExoTiC-LD v3.0.0, Zenodo, doi:10.5281/zenodo.7437681
- Gray, R. O., & Corbally, C. J. 1994, *AJ*, **107**, 742
- Griffin, R. F. 1992, *Obs*, **112**, 41
- Gu, S.-h., Collier Cameron, A., & Kim, K. M. 2010, in *IAU Symp. 264, Solar and Stellar Variability: Impact on Earth and Planets*, ed. A. G. Kosovichev, A. H. Andrei, & J.-P. Rozelot (Cambridge: Cambridge Univ. Press), 90
- Gustafsson, B., Edvardsson, B., Eriksson, K., et al. 2008, *A&A*, **486**, 951
- Harris, C. R., Millman, K. J., van der Walt, S. J., et al. 2020, *Natur*, **585**, 357
- Hunter, J. D. 2007, *CSE*, **9**, 90
- Işık, E., Schmitt, D., & Schüssler, M. 2011, *A&A*, **528**, A135
- Kochukhov, O. 2016, in *Cartography of the Sun and the Stars*, ed. J.-P. Rozelot & C. Neiner, Vol. 914 (Berlin: Springer), 177
- Kolbin, A. I., & Galeev, A. I. 2017, in *ASP Conf. Ser. 510, Stars: from Collapse to Collapse*, ed. Y. Y. Balega et al. (San Francisco, CA: ASP), 417
- Kostogryz, N., Shapiro, A., Witzke, V., et al. 2023, *RNAAS*, **7**, 39
- Kostogryz, N., Witzke, V., Shapiro, A., et al. 2022, *A&A*, **666**, A60

- Kupka, F., Piskunov, N., Ryabchikova, T. A., Stempels, H. C., & Weiss, W. W. 1999, *A&AS*, **138**, 119
- Lehtinen, J., Jetsu, L., Hackman, T., Kajatkari, P., & Henry, G. W. 2016, *A&A*, **588**, A38
- Llorente de Andrés, F., Chavero, C., de la Reza, R., Roca-Fàbrega, S., & Cifuentes, C. 2021, *A&A*, **654**, A137
- López-Santiago, J., Montes, D., Fernández-Figueroa, M. J., & Ramsey, L. W. 2003, *A&A*, **411**, 489
- López-Santiago, J., Montes, D., Gálvez-Ortiz, M. C., et al. 2010, *A&A*, **514**, A97
- Maclaurin, D., Duvenaud, D., & Adams, R. P., 2015 Autograd, <https://github.com/HIPS/autograd>
- Montes, D., Fernández-Figueroa, M. J., De Castro, E., et al. 2000, *A&AS*, **146**, 103
- Montes, D., López-Santiago, J., Fernández-Figueroa, M. J., & Gálvez, M. C. 2001a, *A&A*, **379**, 976
- Montes, D., López-Santiago, J., Gálvez, M. C., et al. 2001b, *MNRAS*, **328**, 45
- Montes, D., López-Santiago, J., Fernández-Figueroa, M. J., & Ramsey, L. W. 2004, in IAU Symp. 219, Stars as Suns: Activity, Evolution and Planets, ed. A. K. Dupree & A. O. Benz (San Francisco, CA: ASP), 915
- Prša, A., Conroy, K. E., Horvat, M., et al. 2016, *ApJS*, **227**, 29
- PyQT, 2012 PyQt, <https://www.riverbankcomputing.com/software/pyqt/>
- Ramachandran, P., & Varoquaux, G. 2011, *CSE*, **13**, 40
- Raskin, G., van Winckel, H., Hensberge, H., et al. 2011, *A&A*, **526**, A69
- Ricker, G. R., Winn, J. N., Vanderspek, R., et al. 2015, *JATIS*, **1**, 014003
- Schöfer, P. 2021, PhD thesis, Georg August Univ. of Göttingen
- Şenavcı, H. V., Bahar, E., Montes, D., et al. 2018, *MNRAS*, **479**, 875
- Strassmeier, K. G., & Rice, J. B. 2006, *A&A*, **460**, 751
- Valenti, J. A., & Piskunov, N. 1996, *A&AS*, **118**, 595
- Virtanen, P., Gommers, R., Oliphant, T. E., et al. 2020, *NatMe*, **17**, 261
- Zhang, L.-Y., Pi, Q.-F., & Zhu, Z.-Z. 2015, *RAA*, **15**, 252
- Zhu, C., Byrd, R. H., Lu, P., & Nocedal, J. 1997, *ACM Trans. Math. Softw.*, **23**, 550